PHYSICAL REVIEW D VOLUME 56, NUMBER 9 1 NOVEMBER 1997

$Z\gamma H$ vertex effects in Higgs-boson production at future $e\gamma$ linear colliders

E. Gabrielli*
University of Notre Dame, Notre Dame, Indiana 46556

V. A. Ilyin†
Institute of Nuclear Physics, Moscow State University, Russia

B. Mele‡
INFN, Sezione di Roma 1 and Rome University ''La Sapienza,'' Italy

(Received 25 February 1997; revised manuscript received 13 June 1997)

One-loop production of a Higgs boson in $e\gamma$ collisions at future accelerators is studied via the process $e\gamma\rightarrow eH$, for intermediate Higgs-boson masses. Exact cross sections, including the possibility of longitudinally polarized initial beams, are presented. Confirming previous estimates made in the Weizsäcker-Williams approximation, they are found to be more than 2 orders of magnitude larger than the cross sections for the crossed process $e^+e^-\rightarrow H\gamma$, in the energy range $\sqrt{s}=(0.5-2)$ TeV. We show that, not only does $e\gamma\rightarrow eH$ have a similar potential as the $\gamma\gamma\rightarrow H$ process for testing the one-loop $\gamma\gamma H$ vertex, but, by requiring a final electron tagged at a large angle in $e\gamma\rightarrow eH$, the He production provides an excellent way of testing the $Z\gamma H$ vertex, too. Kinematical distributions for the $e\gamma\rightarrow eH\rightarrow e(b\overline{b})$ process with a tagged final electron are analyzed, and strategies for controlling the main irreducible background are found. Initial-state-radiation effects are checked to be within a few percent. [S0556-2821(97)05919-5]

PACS number(s): 14.80.Bn, 12.15.Lk, 13.88.+e

I. INTRODUCTION

The Higgs-boson sector is a crucial part of the standard model still escaping direct experimental verification. Presently, we know that $m_H\gtrsim 65$ GeV [1]. Once the Higgs boson will be discovered either at the CERN e^+e^- collider LEP 2 or at the CERN Large Hadron Collider (LHC), testing the Higgs-boson properties will be a central issue at future linear colliders. In particular, an e^+e^- collider with center-of-mass (c.m.) energy $\sqrt{s}\simeq(300-2000)$ GeV and integrated luminosity ~ 100 fb^{-1} will allow an accurate determination of the mass, couplings and parity properties of the Higgs particle [2,3]. Two further options are presently considered for a high-energy linear collider, where one or both the initial e^+/e^- beams are replaced by photon beams induced by Compton backscattering of laser light on the high-energy electron beams [4]. Then, one can study high-energy electron-photon and photon-photon collisions, where the initial photons are real, to a good degree monochromatic, and have energy and luminosity comparable to the ones of the parent electron beam [5].

In this paper, we analyze the Higgs-boson production in $e\gamma$ collisions through the process $e\gamma\rightarrow eH$. This channel will turn out to be an excellent means to test both the $\gamma\gamma H$ and $Z\gamma H$ one-loop couplings with high statistics. Possible ways to test the couplings ggH, $\gamma\gamma H$, and $Z\gamma H$ have been extensively studied in the literature. These one-loop vertices, because of the nondecoupling properties of the Higgs boson, are sensitive to the contribution of new particles circulating in the loops, even in the limit $M_{\text{new}}\gg m_H$ [6].

While the ggH vertex [7] can be tested by the Higgs-boson production via gluon-gluon fusion at LHC, a measurement of the $\gamma\gamma H$ and $Z\gamma H$ couplings should be possible by the determination of the branching ratios (B's) for the decays $H\rightarrow\gamma\gamma$ [8,9] and $H\rightarrow\gamma Z$ [10,9] (see also [11]), respectively. The latter statement holds only for an intermediate-mass Higgs boson (i.e., for $90\lesssim m_H\lesssim 140$ GeV), where both $B(H\rightarrow\gamma\gamma)$ and $B(H\rightarrow\gamma Z)$ reach their maximum value, which is $\sim 10^{-3}$.

Another promising way of measuring the $\gamma\gamma H$ coupling for an intermediate-mass Higgs boson will be realized through Higgs-boson production in $\gamma\gamma$ collisions [12,13]. To this end, the capability of tuning the $\gamma\gamma$ c.m. energy on the Higgs-boson mass, through a good degree of the photons monochromaticity, will be crucial for not diluting too much the $\gamma\gamma\rightarrow H$ resonant cross section over the c.m. energy spectrum.

The process $e\gamma\rightarrow eH$, that we consider here, offers a further interesting way of testing both the $\gamma\gamma H$ and $Z\gamma H$ Higgs vertices. Indeed, we will show that, while the γ-exchange $\gamma\gamma H$ contribution is dominant in the total cross section, by requiring a large transverse momentum of the final electron (or Higgs boson), one enhances the Z-exchange $Z\gamma H$ contribution, while keeping the corresponding rate still to an observable level. The further contribution given by the box diagrams with W and Z exchange survives at large angles too, but is relatively less important. Furthermore, while the $\gamma\gamma H$ and $Z\gamma H$ channels increase logarithmically with the c.m. collision energy, the contribution from boxes starts decreasing at $\sqrt{s}\gtrsim 400$ GeV.

A further advantage of the $e\gamma\rightarrow eH$ process with respect

---

*Electronic address: egabriel@wave.phys.nd.edu

†Electronic address: ilyin@theory.npi.msu.su

‡Electronic address: mele@roma1.infn.it

0556-2821/97/56(9)/5945(17)/$10.00

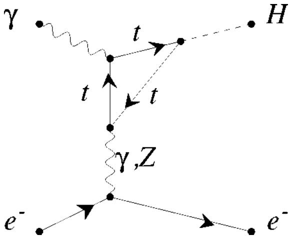

FIG. 1. Feynman diagram with a fermion triangle loop.

to the resonant $\gamma\gamma\to H$ production is that the former is much less crucially dependent on the tuning of the c.m. collision energy to m_H. As a consequence, although the resonant cross section $\sigma_{\rm res}(\gamma\gamma\to H)$ is in general much larger than $\sigma(e\gamma\to eH)$, the effect of the γ-spectrum smearing can make the two rates of the same order of magnitude (see also [13]).

The cross section for the process $e\gamma\to eH$ has previously been studied in the Weizsäcker-Williams (WW) approximation [14], where the only channel contributing is the (almost real) γ exchange in the t channel, induced by the $\gamma\gamma H$ vertex [15] (see also [16], where the pseudoscalar Higgs-boson production is considered). Although, as we will see, this method provides a rather good estimate of the $e\gamma\to eH$ total cross sections, it is unable to assess the importance of the $Z\gamma H$ (and box) effects. This we will address particularly in our exact treatment of $e\gamma\to eH$.

Although cross sections for the process $e\gamma\to eH$ are quite large also for heavy Higgs bosons [e.g., $\sigma(m_H\simeq 400\ \text{GeV})>1$ fb for $\sqrt{s}\gtrsim 500$ GeV], we will concentrate on the intermediate Higgs-boson mass case. Hence, we will carry out a detailed analysis of the main background, assuming that the decay $H\to b\bar{b}$ is dominant.

In principle, the same physics could be tested in the crossed process, $e^+e^-\to H\gamma$, which has been widely studied [17–19]. Unfortunately, the $e^+e^-\to H\gamma$ channel suffers from small rates, which are further depleted at large energies by the $1/s$ behavior of the dominant s-channel diagrams. Also, in this case, it is more difficult to separate the $Z\gamma H$ contribution on the basis of kinematical distributions. As a consequence, if an $e\gamma$ option of the linear collider will be realized with similar luminosity of the e^+e^- option, the $e\gamma\to eH$ channel will turn out to be much more interesting than the process $e^+e^-\to H\gamma$, for finding possible deviations from the standard-model one-loop Higgs vertices.

The plan of the paper is the following. In Sec. II, we present the analytical results for the complete helicity amplitudes of the $e\gamma\to eH$ process. In Sec. III, numerical results for the exact total cross section are given and compared to the ones corresponding to the tree-level Higgs-boson production in $e\gamma\to H\nu_e W$. Also, a discussion of the relative importance of the different one-loop vertices and boxes in $e\gamma\to eH$ is presented. In Sec. IV, the rates for the main background processes are estimated, and strategies for their control are suggested. Initial-beam polarization effects are discussed in Sec. V, while , in Sec. VI, we estimate the influence of the initial state radiation (ISR) on the above picture. In Sec. VII, we discuss the expected precision on a measurement of the $Z\gamma H$ effects through $e\gamma\to eH$, and point out a possible strategy, based on the angular asymmetry of the final electron, for further optimizing the ratio S/B. Finally, in Sec. VIII, we draw our conclusions. In the Appendix, we discuss some technical details of the computation.

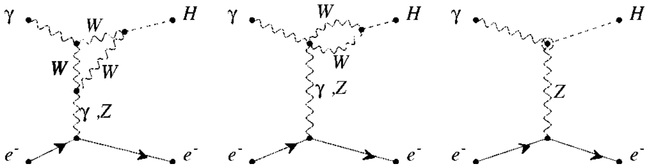

FIG. 2. Feynman diagrams with a W-triangle loop.

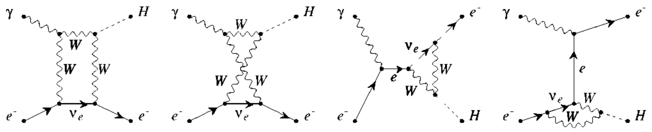

FIG. 3. Subset of Feynman diagrams with a W-box loop and related eeH vertex.

II. HELICITY AMPLITUDES

In this section we give the analytical expression for the matrix element of the process

$$e^-(k_1)\gamma(k_2)\to e^-(k_3)H(k_4) \qquad (1)$$

as a function of the initial electron and photon helicities, where k_i are the particle momenta. We calculate the amplitude in the *'t Hooft–Feynman gauge* and in the chiral limit approximation for the electron mass.

In the *unitary gauge*, the Feynman diagrams which contribute to this process are given in Figs. 1–4 (for the figures of the Feynman diagrams, we used the program GRACEFIG created by Kawabata). In Figs. 1 and 2, we show the fermion and W triangle loops, respectively, with both γ and Z exchanges in the t channel, where in the fermion loop we consider only the contribution of the top quark. To these diagrams, the corresponding ones with opposite orientation for the fermion and W loops have to be added. In Figs. 3 and 4, the W box and Z box, along with the related eeH vertex diagrams, are presented, respectively. The eeH vertex cannot be neglected in the chiral limit, since only the divergent part of this vertex is proportional to the electron mass. Indeed, its finite part is proportional to the momentum square of the off-shell electron, and it is not zero in the chiral limit. Moreover, the finite part of the eeH vertex is needed for the gauge invariance of the total amplitude.

In the 't Hooft–Feynman gauge, we have to add to the first diagram in Fig. 2 the one where the W lines are substituted by the W ghosts. Furthermore, we have to add to the diagrams of Figs. 2 and 3 the ones where the W lines in the

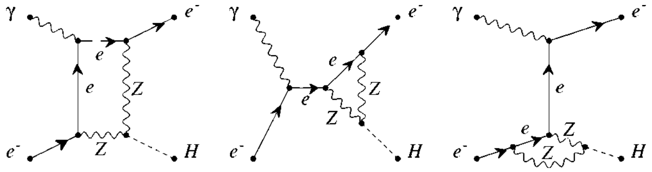

FIG. 4. Subset of diagrams with a Z-box loop and related eeH vertex.

loops are substituted by different combinations of W-boson and W Goldstone boson propagators. For example, there are two diagrams associated with the box diagrams in Fig. 3, where the W propagator not connected with the electron is substituted by a W Goldstone boson propagator. However, starting from the topology of the first two diagrams in Fig. 2, there are new diagrams to add that cannot be generated by the above rule. The latter contain four-leg vertices where the photon interacts with a W Goldstone boson and a Higgs boson, both in the γ and Z t channels. In particular, in the 't Hooft–Feynman gauge, 52 diagrams replace the first two of Fig. 2: 26 with γ exchange plus 26 with Z exchange in the t channel. In the following, when we refer to Figs. 2 and 3, the complete subsets of the corresponding diagrams in the 't Hooft–Feynman gauge are implied.

The third diagram of Fig. 2 is given by the insertion of the vertex $Z\gamma H$ proportional to the counterterm coming from the renormalization of the Z-γ mixing self-energy function at the one-loop level. This diagram is necessary to provide the ultraviolet finiteness of the W-loop contributions. In our calculation, we have used the on-shell renormalization scheme. Hence, explicit contributions from the diagrams with self-energy functions are missing.

The total amplitude for the process (1) is of course QED gauge invariant. This means that, replacing in each diagram the photon polarization vector $e^{\mu}(\lambda,k_2)$ by its momentum k_2^{μ} (here and below $\lambda\equiv P_{\gamma}=\pm 1$ is the photon helicity), the sum over the whole set of diagrams has to vanish. In general, a single diagram (or subset of diagrams) is not transverse in the photon momentum by itself, but we can select the nontransverse part by just taking the terms that do not vanish after this substitution. Then, we find that it is possible to divide the whole set of diagrams into a few QED gauge-invariant subsets of diagrams: (i) fermion loops with γ in the t channel (Fig, 1); (ii) fermion loops with Z in the t channel (Fig. 1); (iii) W-triangle loops (Fig. 2) + W boxes and related eeH vertices (Fig. 3); (iv) Z box and related eeH vertices (Fig. 4). Below, we will see that the W-triangle and W-box diagrams give rise to QED gauge noninvariant terms that cancel in the sum.

In order to get the analytical expression for the amplitude as a function of the initial particle helicities, we decompose the Feynman amplitude in terms of the so-called *standard matrix elements* defined as

$$M_1(\sigma,\lambda)\equiv\overline{u^{\sigma}}(k_3)\hat{e}(\lambda)u^{\sigma}(k_1),$$

$$M_2(\sigma,\lambda)\equiv\overline{u^{\sigma}}(k_3)\hat{k}_2u^{\sigma}(k_1)\cdot(e(\lambda,k_2),k_3), \tag{2}$$

$$M_3(\sigma,\lambda)\equiv-\overline{u^{\sigma}}(k_3)\hat{k}_2u^{\sigma}(k_1)\cdot(e(\lambda,k_2),k_1).$$

Here $u^{\sigma}(k)$ denotes a spinor state for electrons with helicity $\sigma/2$ ($\sigma\equiv P_e=\pm 1$) and momentum k ($\hat{k}=k^{\mu}\gamma_{\mu}$, where γ_{μ} are the Dirac's γ matrices). Note that these elements contain the complete information about the polarizations of the initial electrons and photons.

The amplitude can be expressed in terms of the standard matrix elements in the center-of-mass system (c.m.s.), where the latter become[1]

$$M_1(\sigma,\lambda)=-\sqrt{-\frac{t}{2}}(1+\sigma\lambda),$$

$$M_2(\sigma,\lambda)=\sqrt{-\frac{t}{2}}\,u,\quad M_3(\sigma,\lambda)=0 \tag{3}$$

with the Mandelstam variables defined as

$$s=(k_1+k_2)^2,\quad t=(k_1-k_3)^2,\quad u=(k_2-k_4)^2. \tag{4}$$

The last equality in Eq. (3) is due to the orthogonality in the c.m.s. of the photon polarization vector $e(\lambda,k_2)$ and the electron momentum k_1. Nevertheless, we calculate the coefficients of M_3, too. These coefficients will be useful for the analysis of the QED gauge invariance of the result. Moreover, they will help us to get more compact analytical answers.

The amplitude corresponding to each diagram can be expressed in the form

$$M_1(\sigma,\lambda)\cdot\mathcal{B}_1+M_2(\sigma,\lambda)\cdot\mathcal{B}_2+M_3(\sigma,\lambda)\cdot\mathcal{B}_3, \tag{5}$$

where the coefficients $\mathcal{B}_i$ include the loop integrals. The transversality in the photon momentum implies a linear relation between the coefficients $\mathcal{B}_i$ for the QED gauge-invariant sector of each diagram or subset of diagrams. In fact, after the substitution $e^{\mu}\rightarrow k_2^{\mu}$ in the standard matrix elements (2) and then in (5), we find that, for each QED gauge-invariant subset in the amplitude, these coefficients satisfy the identity

$$\mathcal{B}_1-\frac{u}{2}\mathcal{B}_2-\frac{s}{2}\mathcal{B}_3=0. \tag{6}$$

As a consequence, the partial amplitudes can be represented in the following form, where the standard elements are substituted by their explicit values (3):

$$\frac{1}{2}\sqrt{-\frac{t}{2}}\,[(u\mathcal{B}_2-s\mathcal{B}_3)-\sigma\lambda(u\mathcal{B}_2+s\mathcal{B}_3)]. \tag{7}$$

The final result can be further simplified by using the crossing symmetry connecting the process (1) to the crossed one $e^+(k_3)\gamma(k_2)\rightarrow e^+(k_1)H(k_4)$. If we perform a crossing transformation $(s\leftrightarrow u,\sigma\rightarrow-\sigma)$ in the matrix element of the process (1), we get the same function with opposite electric charge and Z charge of the electron (i.e., with $Q_e\rightarrow-Q_e$, and $g_e\rightarrow-g_e$). Of course, for the Z charge the change of the electron helicity has to be taken into account, too. We found that, for the QED gauge-invariant component of each subset of the diagrams represented in Figs. 1–4, this symmetry is fulfilled, which simplifies further our formulas. Indeed, this symmetry implies that the form factor $u\mathcal{B}_2-s\mathcal{B}_3$ is antisymmetric with respect to the substitution $s\leftrightarrow u$, while $u\mathcal{B}_2+s\mathcal{B}_3$ is symmetric (i.e., $\mathcal{B}_2\leftrightarrow\mathcal{B}_3$ for $s\leftrightarrow u$). Then, instead of the

---

[1] The same expressions still hold after a Lorentz boost along the collision axis of the process $e\gamma\rightarrow eH$.

coefficients $\mathcal{B}_2$ and $\mathcal{B}_3$, it is worthwhile to consider the following symmetric and antisymmetric combinations:

$$\mathcal{F}^s \equiv \frac{u\mathcal{B}_2+s\mathcal{B}_3}{2}, \quad \mathcal{F}^a \equiv \frac{u\mathcal{B}_2-s\mathcal{B}_3}{2}. \tag{8}$$

Using the above form factors, our final analytical results can be represented in the compact form

$$\sqrt{-\frac{t}{2}}\,[\mathcal{F}^a-\sigma\lambda\mathcal{F}^s]. \tag{9}$$

Note that all the dependence on the photon helicity is concentrated in the explicit factor of the second term in Eq. (9). Hence, when one averages over the photon helicity, the dependence on the electron helicity arises only from the $Ze\bar{e}$ coupling. Since $g_e^-\simeq-0.658$ and $g_e^+\simeq0.538$, the Z t-channel contributions have opposite signs in the amplitudes for left-handed and right-handed electrons. Moreover, in the region of large transverse momentum, there is a moderate difference between the γ and Z t-channel propagators. This explains the destructive interference of the γ and Z t channels for a right-handed electron beam, and the mutual enhancement of these contributions in the case of left-handed electrons, when the photon beam is unpolarized (see also Sec. V).

Because of the crossing symmetry for $s\leftrightarrow u$, one has $\mathcal{B}_2=\mathcal{B}_3$ in Eq. (5), for all the triangle amplitudes. This means that, for this class of diagrams, the formula (9) can be further simplified into

$$\frac{1}{2}\Lambda(\sigma,\lambda)\cdot\mathcal{T}, \tag{10}$$

where $\mathcal{T}=\mathcal{B}_2=\mathcal{B}_3$ and

$$\Lambda(\sigma,\lambda)\equiv\sqrt{-\frac{t}{2}}\,[(u-s)-\sigma\lambda(u+s)]. \tag{11}$$

Finally, the differential cross section for the process with longitudinally polarized photon and electron beams[2] is given by

$$\frac{d\sigma(e\gamma\to eH)}{d\Omega}=\frac{1-m_H^2/s}{64\pi^2 s}(\alpha^2 M_Z)^2|M(\sigma,\lambda)|^2, \tag{12}$$

where Ω is the spherical scattering angle of the final electron, and the analytical expression for the total QED gauge-invariant matrix element can be expressed as

$$\begin{aligned}\mathcal{M}(\sigma,\lambda)=&\,\mathcal{M}_{\triangle^f_\gamma}(\sigma,\lambda)+\mathcal{M}_{\triangle^f_Z}(\sigma,\lambda)+\mathcal{M}_{\triangle^W_{\gamma,1}}(\sigma,\lambda)\\&+\mathcal{M}_{\triangle^W_{\gamma,2}}(\sigma,\lambda)+\mathcal{M}_{\triangle^W_{Z,1}}(\sigma,\lambda)+\mathcal{M}_{\triangle^W_{Z,2}}(\sigma,\lambda)\\&+\mathcal{M}_{\square_W}(\sigma,\lambda)+\mathcal{M}_{\square_Z}(\sigma,\lambda).\end{aligned} \tag{13}$$

The partial amplitudes $\mathcal{M}_i$ are given by the following QED gauge-invariant contributions.

Triangle fermion loops:

$$\begin{aligned}\mathcal{M}_{\triangle^f_{(\gamma,Z)}}(\sigma,\lambda)=&\,\frac{m_t^2}{M_Z^2}N_c\frac{Q_t}{s_wc_w}\\&\times\mathcal{P}^f_{(\gamma,Z)}\cdot\Lambda(\sigma,\lambda)\cdot[\mathcal{T}_1(m_t)-2\mathcal{T}_2(m_t)],\end{aligned} \tag{14}$$

$$\mathcal{P}^f_\gamma=\frac{2Q_eQ_t}{-t}, \quad \mathcal{P}^f_Z=\frac{g_e^\sigma(g_t^++g_t^-)}{-t+M_Z^2}.$$

Here, $\mathcal{M}_{\triangle^f_\gamma}$ and $\mathcal{M}_{\triangle^f_Z}$ represent the contributions of the γ and Z t channels, respectively. In the above formulas, $N_c=3$ is the color weight of the t quark, while the electric and Z charges of the fermions, Q_f and $g_f^\pm$, are given by

$$Q_e=-1, \quad g_e^+=-Q_e\frac{s_w}{c_w}, \quad g_e^-=-\frac{1/2+Q_es_w^2}{s_wc_w},$$

$$Q_t=\frac{2}{3}, \quad g_t^+=-Q_t\frac{s_w}{c_w}, \quad g_t^-=\frac{1/2-Q_ts_w^2}{s_wc_w}.$$

Also, $s_w\equiv\sin\theta_W$ and $c_w\equiv\cos\theta_W$, with θ_W the Weinberg angle.

The expressions for the one-loop form factors $\mathcal{T}_1(m)$ and $\mathcal{T}_2(m)$ are given by

$$\mathcal{T}_1(m)\equiv C_0(m,-k_4,m,k_3-k_1,m),$$

$$\begin{aligned}\mathcal{T}_2(m)\equiv&\,\frac{1}{s+u}\left\{2m^2\cdot\mathcal{T}_1(m)+\frac{t}{s+u}\cdot[B_0(t,m^2,m^2)\right.\\&\left.-B_0(m_H^2,m^2,m^2)]-1\right\},\end{aligned} \tag{15}$$

where the functions C_0 and B_0 are defined in the Appendix.[3] The form factors $\mathcal{T}_1(m)$ and $\mathcal{T}_2(m)$ can also be expressed in terms of elementary functions (see [8,9]).

Triangle-W loops:

$$\mathcal{M}_{\triangle^W_{(\gamma,Z),1}}(\sigma,\lambda)=\frac{m_H^2}{M_Z^2}\frac{1}{s_wc_w}\mathcal{P}^W_{(\gamma,Z),1}\cdot\Lambda(\sigma,\lambda)\cdot[\mathcal{T}_2(M_W)], \tag{16}$$

$$\mathcal{P}^W_{\gamma,1}=\frac{Q_e}{-t}, \quad \mathcal{P}^W_{Z,1}=\frac{g_e^\sigma(1-2s_w^2)}{2s_wc_w}\cdot\frac{1}{-t+M_Z^2}.$$

The terms $\mathcal{M}_{\triangle^W_{(\gamma,Z),1}}$ include the loop with the W Goldstone boson propagators only. Three diagrams contribute both in the photon and Z exchange. The presence of terms propor-

---

[2] Of course, the unpolarized cross section can be obtained by averaging over the helicity of the initial particle(s).

[3] Note that, in the limit $t\to0$, the B_0 integrals do not contribute due to the factor t in Eq. (15). Hence, the C_0 integrals give the dominant contribution to the total cross section.

tional to m_H^2/M_Z^2 is a consequence of the Higgs mechanism and the decoupling of the longitudinal components of the W boson at high energy.

$$\mathcal{M}_{\triangle^W_{(\gamma,Z),2}}(\sigma,\lambda)=\frac{c_w}{s_w}\mathcal{P}_{(\gamma,Z),2}\cdot\Lambda(\sigma,\lambda)\cdot[-A_1^{(\gamma,Z)}\mathcal{T}_1(M_W)+A_2^{(\gamma,Z)}\mathcal{T}_2(M_W)],\tag{17}$$

$$\mathcal{P}^W_{\gamma,2}=\frac{Q_e}{-t},\quad A_1^\gamma=8,\quad A_2^\gamma=6,$$

$$\mathcal{P}^W_{Z,2}=\frac{g_e^\sigma}{-t+M_Z^2},\quad A_1^Z=6\frac{c_w}{s_w}-2\frac{s_w}{c_w},\quad A_2^Z=5\frac{c_w}{s_w}-\frac{s_w}{c_w}.$$

The terms $\mathcal{M}_{\triangle^W_{(\gamma,Z),2}}$ include the contribution of the W-triangle diagrams with W ghosts and with a mixture of W bosons and W Goldstones bosons running in the loop. In the $\mathcal{M}_{\triangle^W_{Z,2}}$ term, we also include the diagram with the $Z\gamma H$ counterterm.

W and Z boxes with related eeH vertices:

$$\mathcal{M}_{\Box_{(W,Z)}}(\sigma,\lambda)=\frac{\mathcal{P}^{\Box}_{(W,Z)}}{s_wc_w}\sqrt{-\frac{t}{2}}\cdot[\mathcal{D}^a_{(W,Z)}-\sigma\lambda\mathcal{D}^s_{(W,Z)}],\tag{18}$$

$$\mathcal{P}^{\Box}_W=-2\frac{c_w^2}{s_w^2}\delta_e^\sigma,\quad \mathcal{P}^{\Box}_Z=4(g_e^\sigma)^2Q_e,$$

where $\delta_e^+=0$, $\delta_e^-=1$, and the form factors $D^{s,a}_{(W,Z)}$ are the symmetric and antisymmetric parts of the functions

$$\mathcal{D}_W\equiv u(D_3^W+D_{23}^W+\tilde{D}_1^W-\tilde{D}_{12}^W-\tilde{D}_{22}^W),\tag{19}$$

$$\mathcal{D}_Z\equiv u(D_{12}^Z+D_{22}^Z)$$

under the crossing $s\leftrightarrow u$ symmetry transformation. The functions $D_i^{(W,Z)}$ appearing in Eqs. (19) contain the results of the box loop integrals, and are related to the integrals defined in the Appendix in the following way:

$$D_i^W=D_i(0,k_1,M_W,k_1+k_2,M_W,k_3,M_W),\quad \tilde{D}_i^W=D_i^W|_{s\leftrightarrow u},\tag{20}$$

$$D_i^Z=D_i(m_e,k_2,m_e,k_2-k_3,M_Z,-k_1,M_Z).\tag{21}$$

In the Z-box functions in Eq. (21), we restore the electron mass since the integrals D_i are not separately finite for $m_e=0$. Of course, the total amplitude has to be insensitive to the value of m_e used to regularize each singular Z-box integral. We checked the stability of the total result numerically, for a wide range of m_e, going from 10^{-34} GeV up to its physical value.

In the following sections, we refer to the different QED gauge-invariant contributions defined above as

‘‘$\gamma\gamma H$’’ corresponding to $\mathcal{M}_{\triangle^f_\gamma}+\mathcal{M}_{\triangle^W_{\gamma,1}}+\mathcal{M}_{\triangle^W_{\gamma,2}}$,
‘‘$Z\gamma H$’’ corresponding to $\mathcal{M}_{\triangle^f_Z}+\mathcal{M}_{\triangle^W_{Z,1}}+\mathcal{M}_{\triangle^W_{Z,2}}$,
‘‘box’’ corresponding to $\mathcal{M}_{\Box_W}+\mathcal{M}_{\Box_Z}$.

For completeness, we now show the analytical results for the QED gauge noninvariant terms, arising from the W-triangle and W-box diagrams. As we checked, the sum of these terms vanishes. They can be worked out by calculating all the coefficients $\mathcal{B}_i$ and then performing the substitutions $e(\lambda,k_2)\rightarrow k_2$ in Eq. (5). From the W-triangle diagrams, we obtain, for such terms,

$$\mathcal{M}_{\triangle^W_{(\gamma,Z),3}}(\sigma,\lambda)=\frac{c_w}{s_w}\mathcal{P}_{(\gamma,Z),3}\cdot[\mathcal{K}_{(\gamma,Z)}\cdot M_1(\sigma,\lambda)\cdot\mathcal{T}_1(M_W)],\tag{22}$$

$$\mathcal{P}_{\gamma,3}=-\frac{Q_e}{-t},\quad \mathcal{P}_{Z,3}=\frac{c_wg_e^\sigma}{s_w}\cdot\frac{1}{-t+M_Z^2}.$$

In Eq. (22), the coefficients $\mathcal{K}_{(\gamma,Z)}$, arising from the W-triangle diagrams with W ghosts and with a mixture of W bosons and W Goldstone bosons running in the loop, are given by

$$\mathcal{K}_\gamma=3t,\quad \mathcal{K}_Z=3(-t+M_Z^2),\tag{23}$$

and cancel the corresponding γ and Z propagators. After summing the two terms in Eq. (22), we obtain

$$\mathcal{M}_{\triangle^W_{(\gamma+Z),3}}(\sigma,\lambda)=\frac{c_w\delta_e^\sigma}{2s_w^3}[-3M_1(\sigma,\lambda)\cdot\mathcal{T}_1(M_W)].\tag{24}$$

This term is exactly cancelled by an opposite term coming from the QED gauge noninvariant contribution of the W-box diagrams (Fig. 3). We stress that the eeH-vertex diagrams must be added to the W-box diagrams in order to fulfill the QED gauge-invariance identity (6) for this subset of diagrams, after the cancellation of the term (24). Note that the eeH-vertex diagrams contribute through the $\mathcal{B}_1$ coefficients to the weight of the standard matrix element M_1 (2). In the case of the Z-box diagram (Fig. 4), the identity (6) is fulfilled automatically when one adds the corresponding eeH-vertex diagrams.

We checked that our expressions for the one-loop form factors agree with that of [17–19], where the crossed process $e^+e^-\to\gamma H$ was investigated. We also checked that our loop form factors $\mathcal{B}_i$ are in agreement with the corresponding loop form factors for the process $e^+e^-\to HZ$ in [20], if the proper crossing transformation is made and the Z vertices are replaced by the related γ vertices.

Some comments on the gauge dependence of our decomposition in $\gamma\gamma H$, $Z\gamma H$, and box contributions of Eq. (13) are in order. By construction, the identity (6), which is equivalent to the photon transversality, is fulfilled by these contributions separately. One can check that our decomposition corresponds to the $\gamma\gamma H$, $Z\gamma H$, and $e^+e^-\gamma H$ Green's functions in the so-called nonlinear gauge, where the derivative in the 't Hooft–Feynman gauge for the W field is replaced by the corresponding covariant derivative. It has been shown [17] that, in this gauge, the Slavnov-Taylor identities for the $\gamma\gamma H$ and $Z\gamma H$ Green's functions are simply equivalent to the transversality with respect to the photon momenta.

Here, we want to stress, first of all, some technical advantages of the proposed calculation method, based on exploiting the transversality identity (6). Indeed, we chose the widely used 't Hooft–Feynman gauge, and decomposed the Feynman amplitudes in terms of a set of standard matrix elements. We used the set (2), although this choice is not unique. Then, using the transversality of the physical amplitudes, we found that the coefficients of the standard matrix elements have to fulfill some linear identity, that in our case is Eq. (6). Accordingly, one can take any partial contribution, for example, the contribution of different subsets of diagrams, then calculate only the terms satisfying this linear identity, and ignore the violating terms. As a consequence, as we showed, this technique helps getting more compact answers for the physical amplitudes. We stress the generality of the proposed technique. For comparison, we refer to the paper [19], where the same (QED gauge invariant) contributions to the crossed process $e^+e^-\to\gamma H$ were obtained by choosing an *ad hoc* special set of standard matrix elements.

There is another advantage of the adopted decomposition. Our main goal here is to demonstrate the usefulness of the process $e\gamma\to eH$ for measuring the $Z\gamma H$ coupling. Of course, one does not expect that the contribution of the Z-boson vertices can be separated from the related photon vertices in an SU(2) gauge-invariant way in the standard model. This connects with the presence of the third component of the SU(2) gauge field in both the Z-boson and photon fields. Moreover, one can show that even the box contribution cannot be isolated in a SU(2) gauge-invariant way, by comparing the results in the linear 't Hooft–Feynman gauge used here, with the nonlinear gauge results (see details in [17]). However, we will see in the next section that the contribution of the box diagrams to the cross section is in general rather small. Hence, the most important issue is the separation of the $Z\gamma H$and $\gamma\gamma H$ vertices. In general, if one wants to compare the relative contributions of the $Z\gamma H$and $\gamma\gamma H$ vertices, one needs to specify the gauge in which one works.

Note that it is possible that there are new nonstandard particles circulating in the loops of the $Z\gamma H$ and $\gamma\gamma H$ Green's functions, giving additional contributions to the ones of the standard-model electroweak theory. Hence, measuring the corresponding amplitudes could give us some hints on the nature of the actual extension of the standard model.

In case the new scenario implies the nondecoupling regime for the Higgs-boson interaction with the new particles, we can use an effective pointlike interaction Lagrangian to calculate the contributions of the new physics. In [21,22], the relevant Lagrangian terms were classified and parametrized using five anomalous coupling constants. Of course, these terms must be SU(2)×U(1) gauge invariant, and, hence, transversal with respect to the photon momentum. The same is true for their contributions to the $Z\gamma H$ and $\gamma\gamma H$ Green's functions and to the cross section of the process under discussion. As a consequence, from a kinematical point of view, this type of new physics would contribute similarly to the QED gauge-invariant contributions of the standard $Z\gamma H$ and $\gamma\gamma H$ Green's functions. Thus, our strategy in the next sections will be to find out the kinematical regions where the relative contribution of the transversal $Z\gamma H$ Green's function is enhanced in comparison with the $\gamma\gamma H$ one.

Alternative cases, where the Higgs boson interacts with the new particles in the decoupling limit, cannot be described by an effective pointlike Lagrangian, and some different strategy is necessary to extract the contributions of the corresponding $Z\gamma H$ and $\gamma\gamma H$ induced vertices (see [11], for the case of the minimal supersymmetrical extension of the standard model). In these cases, there could be some kind of common agreement to define the different contributions. For instance, our decomposition in Eq. (13) could do the job. Consequently, the analysis of the numerical results and kinematical cuts made in the following should be of some help for the measurement of the $Z\gamma H$ induced vertex in decoupling cases, too.

III. EXACT CROSS SECTIONS

In this section, we present the total rates $\sigma(He)$ for the process $e\gamma\to eH$ versus the Higgs boson mass m_H and the c.m. $e\gamma$ collision energy $\sqrt{s}$. We also compare them with the cross sections for the competing tree-level process $e\gamma\to H\nu_e W$ [23]. A possible strategy for enhancing the $Z\gamma H$ vertex effects with respect to the dominant $\gamma\gamma H$ contribution is then outlined.

In order to correctly relate our exact results to the previous approximate estimates, one should take into account that in our paper we always assume an exactly monochromatic initial photon beam. It has been customary for some time to present total rates convoluted with a particular form of the initial-photon energy spectrum [4]. On the other hand, presenting unfolded results can help in distinguishing the physical effects related to the particular collision process from details depending on the final realization of the backscattered laser beam, that could evolve with time before the final project of the linear collider is approved.[4]

In our numerical results, we assume $\alpha(m_e)=1/137$ in each vertex that involves an on-shell (or almost on-shell) photon. On the other hand, we express both purely electroweak vertices and vertices involving off-shell photons (exchanged in the t channel when $p_T^H\gtrsim 10$ GeV) in terms of

---

[4] That was recently stressed by Telnov [24].

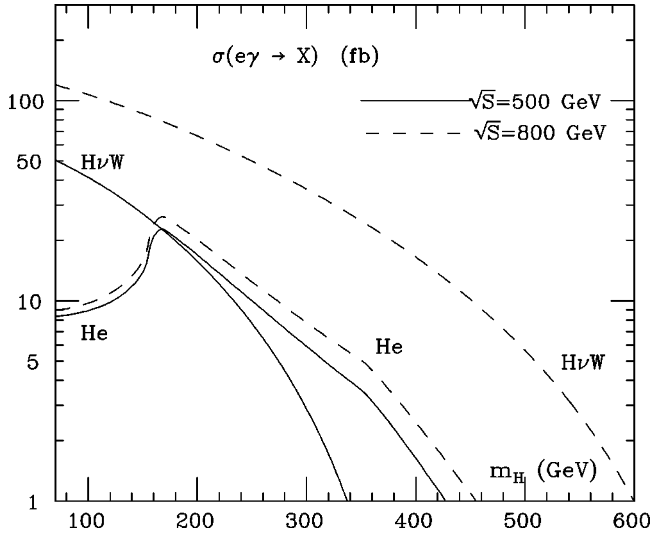

FIG. 5. Total cross sections for the two main H production processes.

$\alpha(M_W)=1/128$. This is made in a gauge-invariant way, i.e., by just rescaling the final cross sections. Also, we assumed M_Z=91.187 GeV, $\sin^2\theta_W$=0.2247, and, for the top-quark and b-quark masses, $m_t=175$ GeV and $m_b=4.3$ GeV, respectively.

In Fig. 5, the total (unpolarized) cross sections for the one-loop process $e\gamma\to eH$ (obtained by integrating the analytical formulas in Sec. II) and the tree-level Higgs-boson production $e\gamma\to H\nu_e W$ (computed by CompHEP [25]) are plotted versus m_H, for $\sqrt{s}=500$ and 800 GeV. Numerical results can also be found in Table I, where the m_H dependence of the two channels is reported for $\sqrt{s}=$ 0.5, 1, and 1.5 TeV.

One can see that the process $e\gamma\to eH$ is characterized by relatively large rates. For instance, for m_H up to about 400 GeV, one finds $\sigma(He)>1$ fb, which, for an integrated luminosity of about 100 fb^{-1}, corresponds to more than 100 events. Note also that the cross section for the crossed process $e^+e^-\to H\gamma$ has a similar behavior with m_H, but is only about a fraction $(\frac{1}{200}-\frac{1}{400})$ of $\sigma(He)$, in the range $m_H=(100-400)$ GeV at $\sqrt{s}=500$ GeV [19]. Moreover, contrary to $\sigma(He)$, $\sigma(H\gamma)$ drops as $1/s$ at large c.m. collision energies .

At $\sqrt{s}\simeq 500$ GeV, the $e\gamma\to eH$ rate increases with m_H up to $m_H\simeq 2M_W$, where $\sigma(He)\simeq 21$ fb. For larger masses, the cross section falls, but more slowly than in the $\sigma(H\nu W)$ case. As a result, $\sigma(He)>\sigma(H\nu W)$ for $m_H\gtrsim 180$ GeV.

At larger $\sqrt{s}$, $\sigma(He)$ increases, but only slightly. On the other hand, $\sigma(H\nu W)$ takes great advantage by a larger c.m. collision energy and, e.g., at $\sqrt{s}=1$ TeV and $m_H=180$ GeV, is more than a factor 4 larger than the corresponding $e\gamma\to eH$ cross section (cf. Table I).

We also compared the exact rates for $e\gamma\to eH$ with the rates one obtains in the Weizsäcker-Williams (WW) approximation according to the approach of [15]. We have found that the WW approximation differs from the exact rate by

TABLE I. Total cross sections in fb. The bottom part of the table is a comparison of the signal with the irreducible background $e\gamma\to eb\bar{b}$ and the reducible background coming from $e\gamma\to ec\bar{c}$, for different e-beam polarizations. For the $e\gamma\to ec\bar{c}$ background a 10% probability of misidentifying a c quark into a b is assumed (that is, only 1/10 of the cross section is reported). Two configurations for kinematical cuts are considered. The angular cut $\theta[b(c)-\text{beam}]>18°$ is applied everywhere. The signal rates include the complete treatment of the $H\to b\bar{b}$ decay. The $b\bar{b}$ invariant mass for the background is integrated over the range $m_H-\Delta m_{b\bar{b}}<m_{b\bar{b}}(m_{c\bar{c}})<m_H+\Delta m_{b\bar{b}}$ with $\Delta m_{b\bar{b}}=3$ GeV.

m_H	$\sqrt{s}=0.5$ TeV		$\sqrt{s}=1$ TeV		$\sqrt{s}=1.5$ TeV	
(GeV)	$e\gamma\to eH$	$e\gamma\to\nu WH$	$e\gamma\to eH$	$e\gamma\to\nu WH$	$e\gamma\to eH$	$e\gamma\to\nu WH$
80	8.48	47.3	9.34	157	9.78	243
100	8.96	41.3	10.0	148	10.5	233
120	9.93	35.4	11.2	138	11.8	223
140	12.0	29.8	13.8	129	14.6	212
160	21.4	24.6	25.1	120	26.7	201
180	21.2	19.9	25.4	111	27.1	191
200	17.5	15.7	21.4	102	22.9	181
300	6.11	2.87	8.61	65.4	9.47	136
400	1.69	0.0151	2.84	38.8	3.21	100
500			0.537	20.9	0.614	72.9
600			0.0944	9.51	0.107	51.5
700			0.0685	3.23	0.0967	35.0

$m_H=120$ GeV	$p_T^e>100$ GeV			$p_T^e>10$ GeV		
$\sqrt{s}=500$ GeV	$\sigma(eH)$ (fb)	$\sigma(ebb)$ (fb)	$\sigma(ec\bar{c})$ (fb)	$\sigma(eH)$ (fb)	$\sigma(ebb)$ (fb)	$\sigma(ec\bar{c})$ (fb)
$P_e=0$	0.530	0.634	0.208	1.17	1.34	0.868
$P_e=-1$	1.03	0.961	0.277	1.89	1.94	1.00
$P_e=+1$	0.0249	0.304	0.136	0.422	0.767	0.726

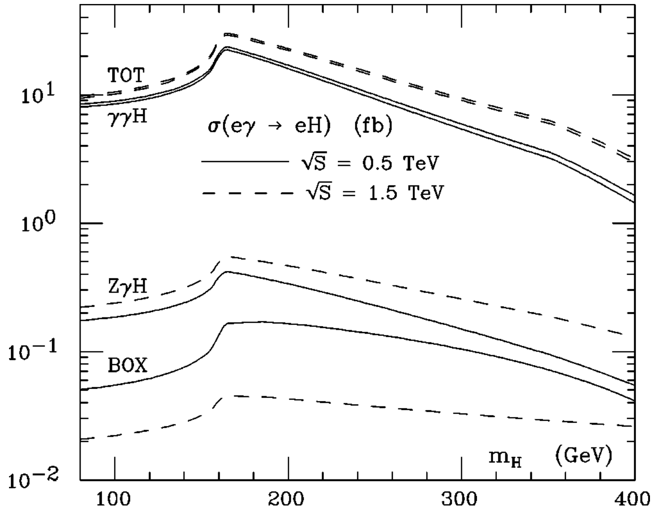

FIG. 6. Total cross section for $e\gamma \rightarrow eH$ plus different partial contributions (see text).

less than 15% in the range $\sqrt{s} = 0.5 - 1.5$ TeV, working better at lower $\sqrt{s}$ and higher m_H. For instance, at $\sqrt{s} = 500$ GeV and $m_H = 300$ GeV, the WW cross section is larger than the exact one by only 3.4%. Anyhow, by adopting an improved WW approach [26], one reaches an accuracy better the 6% in the same $\sqrt{s}$ range.

Note also that the difference in the relative importance of the two channels $e\gamma \rightarrow eH$ and $e\gamma \rightarrow H\nu_e W$ in Fig. 5 with respect to Fig. 1 of [15] is mainly due to the inclusion of a spectrum for the photon beam [4] in the latter case. Indeed, the photon spectrum considered depletes considerably $\sigma(H\nu W)$, while $\sigma(He)$ keeps relatively stable.

In Fig. 6, we show separately the contributions to the total cross section for $e\gamma \rightarrow eH$ given by the squared amplitudes corresponding to the subsets of Feynman diagrams "$\gamma\gamma H$," "$Z\gamma H$," and "box" (defined in Sec. II). Even if this separation is by no means formally rigorous (and neglects the relative interference effects), it can help in getting a feeling of the relative importance of triangular vertices and box contributions to the total cross section. In Fig. 6, the upper solid (dashed) curve corresponds to the total cross section at $\sqrt{s} = 0.5(1.5)$ TeV. The slightly lower curve shows the largely dominant contribution from the $\gamma\gamma H$ vertex graphs, while the $Z\gamma H$ and box cross sections are a factor about 50(45) and 150(500) smaller, respectively, for $m_H \sim 150$ GeV and $\sqrt{s} = 0.5(1.5)$ TeV. At larger m_H, this pattern keeps qualitatively similar.

In principle, the $e\gamma \rightarrow eH$ total cross section (and its main contribution from $\gamma\gamma H$) is of the same order of magnitude of the total rates for Higgs production in $\gamma\gamma$ collisions [13]. Indeed, the expected resolution on the beam energy smears the higher peak cross section over a width much larger than the Higgs resonance. As a result, the channel $e\gamma \rightarrow eH$ has a comparable potential with respect to the process $\gamma\gamma \rightarrow H$ in testing the $\gamma\gamma H$ vertex, as far as the production rates are concerned. In this paper, on the other hand, we would like to concentrate on the problem of disentangling the $Z\gamma H$ vertex effects, which are out of the $\gamma\gamma$-collision domain.

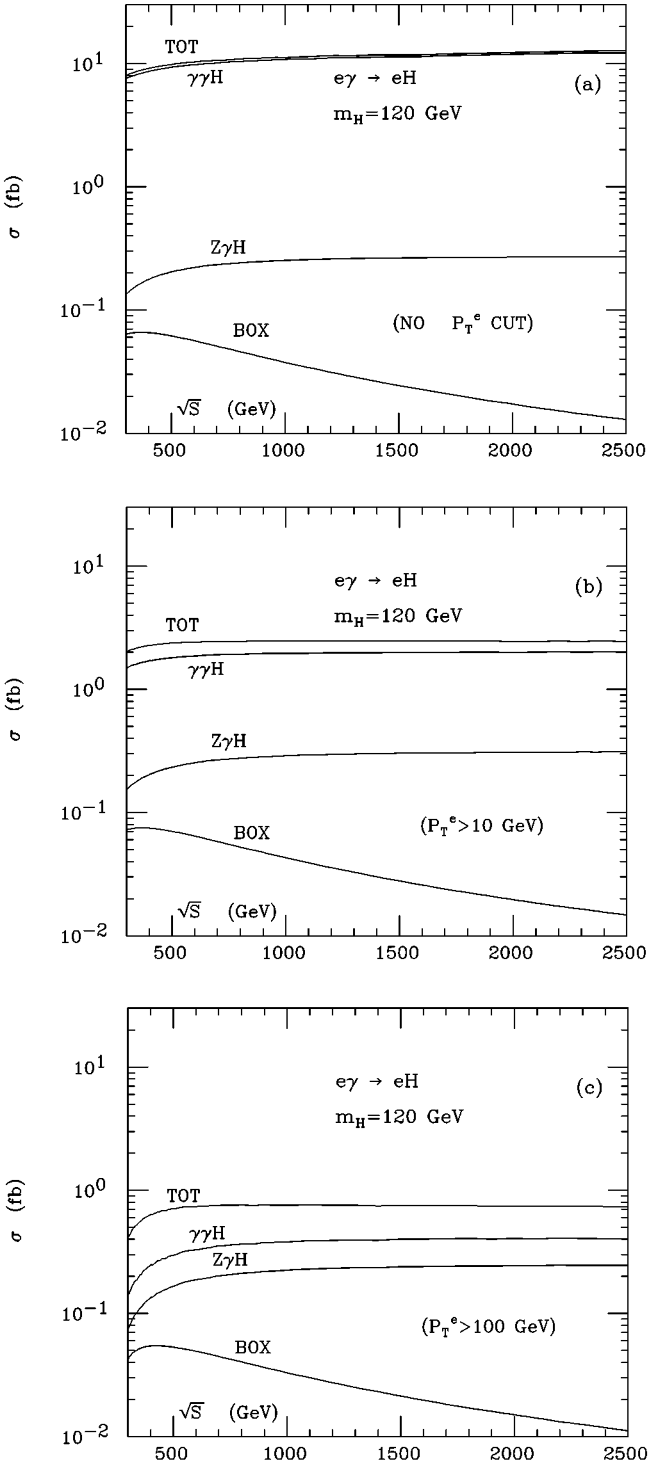

FIG. 7. Effect of varying the p_T^e cut on the $e\gamma \rightarrow eH$ cross section.

In Fig. 7, we show a possible strategy to enhance the $Z\gamma H$ vertex effects in the He production rate. This consists in requiring a final electron (positron) tagged at large angle. The corresponding cut on the transferred squared momentum t depletes mainly the amplitudes involving a photon propagator in the t channel. This can be easily seen from the three plots in Fig. 7, where the cross-section dependence on $\sqrt{s}$, for $m_H = 120$ GeV, is shown for no cut on the electron transverse momentum p_T^e (a), for a cut $p_T^e > 10$ GeV (b), and a cut $p_T^e > 100$ GeV (c). The relative weight of the $Z\gamma H$ and box contributions with respect to the total cross section is consid-

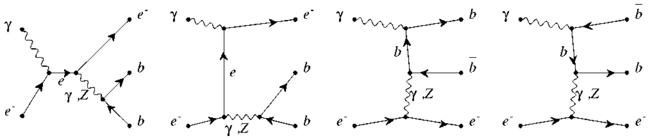

FIG. 8. Diagrams for the $e\gamma\to eb\bar{b}$ background.

erably enhanced by a cut on the minimum allowed p_T^e. For $p_T^e > 100$ GeV, $Z\gamma H$ is about 60% of $\gamma\gamma H$, and $Z\gamma H$ gives a considerable fraction of the total production rate, which is still sufficient to guarantee investigation (about 0.7 fb). One can also notice that the box contribution is of some relevance only in the lower $\sqrt{s}$ range. Note that the slight increase in the $Z\gamma H$ and box "cross sections" when going from Figs. 7(a) to 7(b) is due to the change of a factor $\alpha(m_e)^2$ into $\alpha(M_W)^2$, which, as previously mentioned, we adopt for large-p_T^e configurations.

We stress that, in the inclusive He production, the bulk of the events are characterized by a forward final electron escaping detection. On the other hand, requiring a large p_T^e corresponds, from an experimental point of view, to selecting a different final-state configuration, where the Higgs decay products have a large total transverse momentum, balanced by a high-energy electron detected at large angle.

IV. BACKGROUND PROCESSES

Assuming a final electron tagged at large transverse momentum in $e\gamma\to eH$, we now address the issue of separating the signal coming from an intermediate mass Higgs (i.e., with $90 \lesssim m_H \lesssim 140$ GeV) from the most important background channels. We recall that the main decay mode for an intermediate mass Higgs boson is through the channel $H\to b\bar{b}$, with a branching fraction of about 85%.

An in-depth discussion of the problem has been presented in [15] in the different case of a collinear (undetected) final electron, where one can adopt the WW approximation approach. As we have already stressed, the latter is not useful for distinguishing $Z\gamma H$ vertex effects.

The main irreducible background to the process $e\gamma\to eH\to e(b\bar{b})$ comes from the channel $e\gamma\to eb\bar{b}$. In the latter, a b quark pair is produced either through the decay of a virtual $\gamma(Z)$ or via the fusion of the initial γ with a (virtual) γ or Z radiated by the electron beam. The complete set of Feynman diagrams is given by eight graphs and is shown in Fig. 8.

A crucial parameter to set the importance of the $e\gamma\to eb\bar{b}$ background is the experimental resolution on the $b\bar{b}$ invariant mass $\Delta m_{b\bar{b}}$. The background rates we present here are obtained by integrating the $m_{b\bar{b}}$ distribution over the range $m_H - \Delta m_{b\bar{b}} < m_{b\bar{b}} < m_H + \Delta m_{b\bar{b}}$. We assume a very good mass resolution on the b quark pair, i.e., $\Delta m_{b\bar{b}} = 3$ GeV. Reaching a good resolution on $m_{b\bar{b}}$ can be actually easier in the eH production at large angle. Indeed, the tagging of the final electron e_f implies the possibility of determining its energy with good accuracy. This reflects into an indirect (additional) determination of $m_{b\bar{b}}$ through the relation

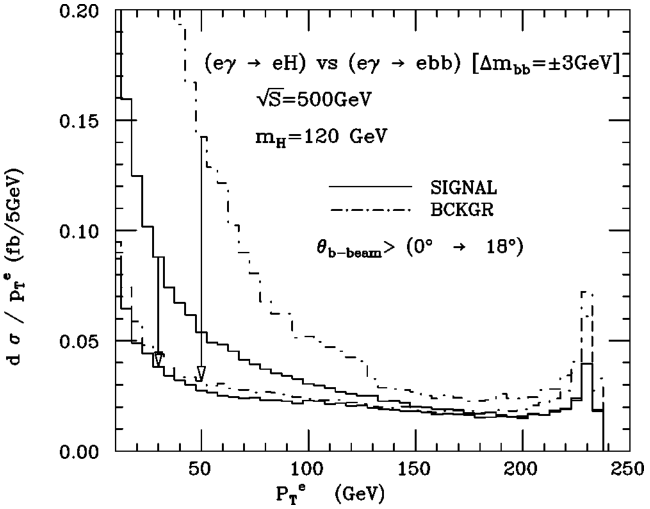

FIG. 9. Distribution in p_T^e for the signal and the background before and after angular cuts on the b's are applied.

$$E(e_f) = \frac{s - m_{b\bar{b}}^2}{2\sqrt{s}}.$$

Assuming a monochromatic photon beam and neglecting ISR effects (i.e., assuming a fixed s), the latter implies a direct connection between the $m_{b\bar{b}}$ resolution and the e_f energy resolution, which can help in improving $\Delta m_{b\bar{b}}$ in the final-state configuration considered here (see also [27]).

We now carry out a detailed analysis of the background from $e\gamma\to eb\bar{b}$. We use CompHEP to generate the kinematical distributions and cross sections. As anticipated, all the rates presented are obtained by integrating the $m_{b\bar{b}}$ distribution over the range $m_H - \Delta m_{b\bar{b}} < m_{b\bar{b}} < m_H + \Delta m_{b\bar{b}}$, with $\Delta m_{b\bar{b}} = 3$ GeV. As for the signal rates, we obtain the distributions for the process $e\gamma\to eH\to e(b\bar{b})$ by convoluting the H distribution for $e\gamma\to eH$ with an isotropic (in the Higgs rest frame) decay $H\to b\bar{b}$, with proper branching ratio. This chain, too, is implemented in a modified version of CompHEP, that generates events according to the exact one-loop matrix element for $e\gamma\to eH$.

In Fig. 9, the upper solid and dot-dashed histograms show the p_T^e distributions for the signal and background, respectively, for $m_H = 120$ GeV and $\sqrt{s} = 500$ GeV. The background is considerably larger than the signal, especially at moderate values of p_T^e. A possible way to improve this picture is by putting a cut on the angles between each b and the initial beams. In fact, the vector couplings that characterize the b's in the channel $e\gamma\to eb\bar{b}$ give rise to a b angular distribution considerably more forward-backward peaked than in the case of the scalar $Hb\bar{b}$ coupling relevant for the signal. In Fig. 9, the arrows show the lowering of the p_T^e distributions, when an angular cut $\theta_{b\ \mathrm{beam}} > 18°$ is applied between each b quark and both the beams. This particular value of the angular cut reduces the signal and background distributions at a comparable level, without penalizing appreciably the signal rate at large p_T^e. Note that the cut $\theta_{b\ \mathrm{beam}} > 18°$ has been optimized at $\sqrt{s} = 500$ GeV. Lower angular cuts will be more convenient at larger $\sqrt{s}$.

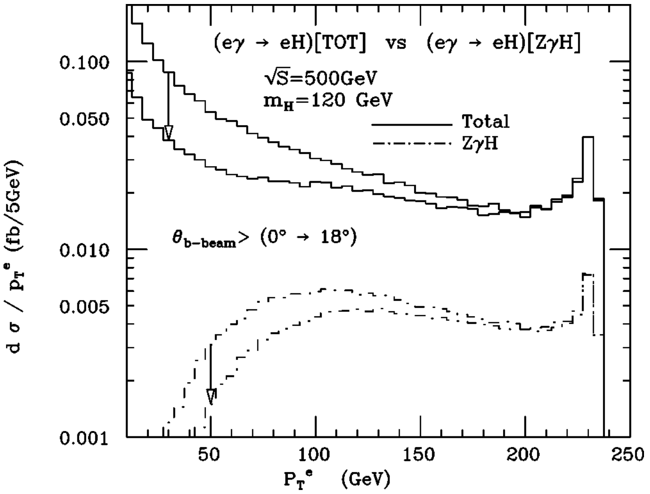

FIG. 10. Same as in the previous figure, for the signal and the $Z\gamma H$ contribution to the signal.

Since, we are interested in isolating $Z\gamma H$ effects, in Fig. 10 we compare the same p_T^e distribution of the signal (and the corresponding effect of the $\theta_{b\ \mathrm{beam}}$ cut) with the distribution coming from the pure squared $Z\gamma H$ amplitude. One can check that the latter is concentrated at large p_T^e values, which is a typical effect of the massive Z propagator in the t channel. The corresponding contribution to the total rate is practically unaltered if one imposes a cut $p_T^e \gtrsim 50$ GeV.

A further source of background for the process $e\gamma \rightarrow eH \rightarrow e(b\bar{b})$ is the charm production through $e\gamma \rightarrow ec\bar{c}$, when the c quarks are misidentified into b's. This reducible background can be cured by a good b-tagging efficiency, that should control a charm production rate that can be even more than a factor 10 larger than the corresponding $e\gamma \rightarrow eb\bar{b}$ cross section, depending on the particular kinematical configuration [15]. We computed the rate for $e\gamma \rightarrow ec\bar{c}$. By assuming a 10% probability of misidentifying a c quark into a b (hence, considering only a fraction 1/10 of the computed $e\gamma \rightarrow ec\bar{c}$ rate), we find that this reducible background has lower rates than the irreducible one. This can be seen in the bottom part of Table I, where the signal is compared with both the reducible and irreducible background, for two different sets of kinematical cuts, that enhance the $Z\gamma H$ contribution, and $m_H = 120$ GeV, at $\sqrt{s} = 500$ GeV. Different initial polarizations for the e beam are considered (see Sec. V). For unpolarized beams and $p_T^e > 100$ GeV, the $e\gamma \rightarrow ec\bar{c}$ ''effective rate'' is less than 1/3 on the $e\gamma \rightarrow eb\bar{b}$ rate. Note that the $e\gamma \rightarrow ec\bar{c}$ channel is kinematically similar to $e\gamma \rightarrow eb\bar{b}$. Hence, the particular strategies analyzed here to reduce the latter automatically deplete also the former.

A further background, that was considered in [15], is the resolved $e\gamma(g) \rightarrow eb\bar{b}$ production, where the photon interacts via its gluonic content. Its estimate depends on the particular assumption for the gluon distribution in the photon that is presently poorly known. We tried anyway to also evaluate this possible background, by assuming that the gluon distribution in the photon beam is given by the parametrization [28] (where we have set the energy scale[5] Q^2 in the structure functions equal to $4m_b^2$). For instance, for the same set of kinematical cuts, and the same m_H and $\sqrt{s}$ values assumed in Table I, bottom half, we have found that $e\gamma(g) \rightarrow eb\bar{b}$ contributes to the background with rates of 9.6×10^{-3} fb and 0.40 fb, for $p_T^e > 100$ and 10 GeV, respectively (and unpolarized beams). We also evaluated the contribution from the c quark production by resolved photons, by $e\gamma(g) \rightarrow ec\bar{c}$. Assuming, as above, a 10% probability of misidentifying a c into a b, and the same kinematical cuts, the corresponding rates are 2.8×10^{-3} fb and 0.16 fb, for $p_T^e > 100$ and 10 GeV, respectively (and unpolarized beams). The rates presented here derive from a leading-order parametrization of the photon structure functions in [28]. We checked that a higher-order parametrization raises the results by at most 10%. Compared to the direct photon contributions reported in Table I, the resolved photon background should hence only marginally alter the signal-to-background ratio, especially at large[6] p_T^e.

In the following, we will restrict to consider the irreducible $e\gamma \rightarrow eb\bar{b}$ background, being confident that, at large values of the p_T^e where the $Z\gamma H$ effects are enhanced, the latter provides the dominant component to the $e\gamma \rightarrow eH$ background.

V. BEAM-POLARIZATION EFFECTS

One of the advantages of a linear collider is the possibility to work with polarized beams. This may allow one, on the one hand, to test the parity structure of the interactions governing a particular process and, on the other hand, to optimize its background suppression. Here, we consider the possibility of having either the electron or the photon beam longitudinally polarized.

In Figs. 11(a) and 11(b), for $m_H = 120$ GeV and versus $\sqrt{s}$, we show the total cross section (and its $\gamma\gamma H$, $Z\gamma H$, and box components) for the unpolarized case (solid) and a completely longitudinally polarized electron (dashed). In particular Fig. 11(a) refers to a left-handed electron beam $(P_e = -1)$, while Fig. 11(b) presents the case of a right-handed electron $(P_e = +1)$. While the $\gamma\gamma H$ curve is unaltered by a $P_e \neq 0$ value, the total cross section is slightly modified by the influence of the electron polarization on the parity nonconserving $Z\gamma H$ and box couplings. In particular, a left- (right-) handed electron beam increases (decreases) σ_{tot}, the $Z\gamma H$ and the box contribution by about 11, 20, and 100 %, respectively, at $\sqrt{s} = 500$ GeV. The strong variation in the box component is produced by the dominance of the W-box sector in this contribution.

In Figs. 11(c) and 11(d), the same plots are given when a cut $p_T^e > 100$ GeV is applied on the final electron transverse

---

[5] This choice of the scale among possible others tends to maximize the resolved-photon rate.

[6] The resolved-photon rates above include only the gluon content of the initial photon beam. The contribution coming from the gluon content of the virtual photon, that can be radiated by the initial electron, is not included here. Anyway this is expected to be less important than the former contribution.

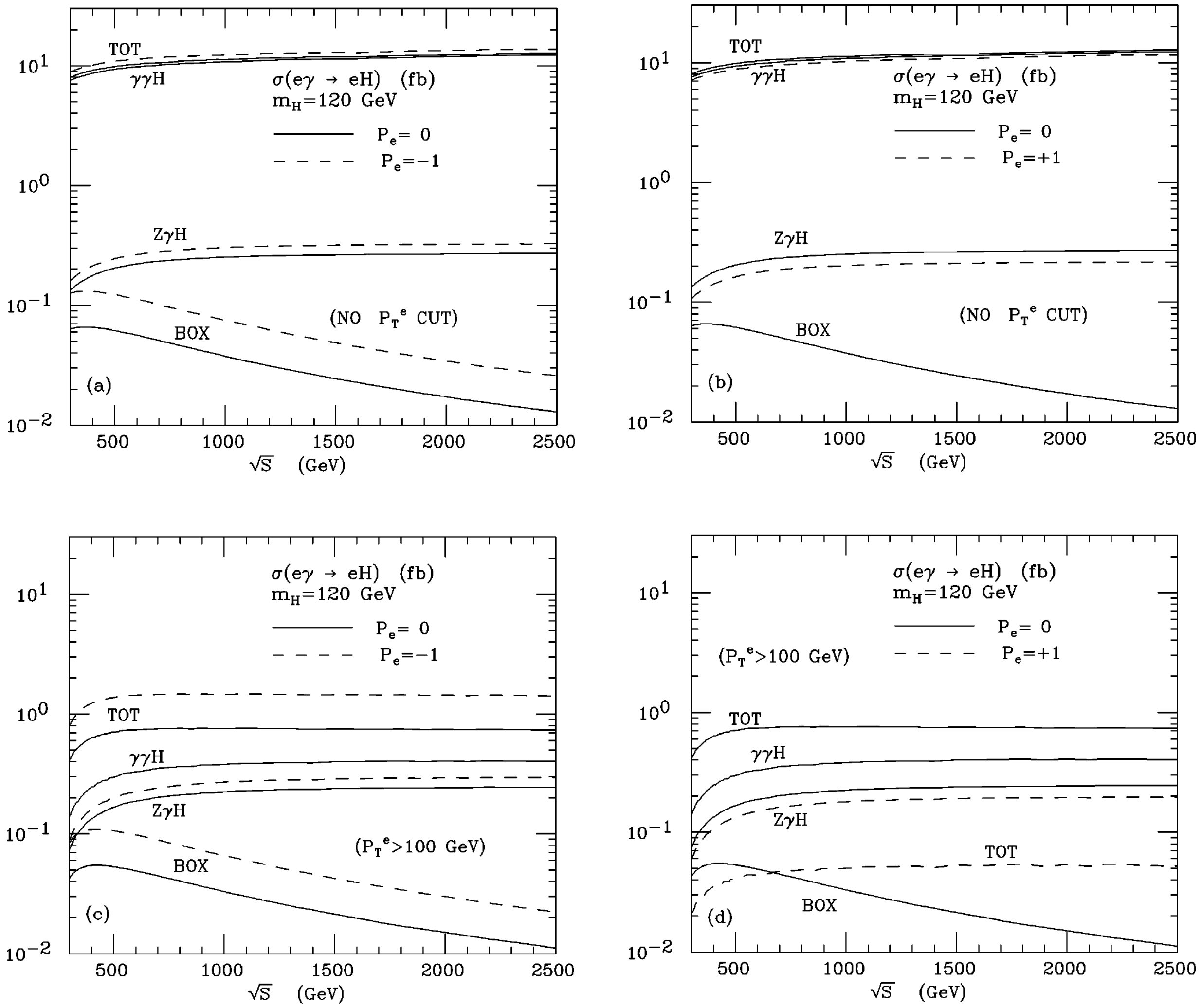

FIG. 11. Electron beam polarization effects without [(a) and (b)] and with [(c) and (d)] a cut $p_T^e > 100$ GeV.

momentum. One can see that in the high-p_T^e sector of the phase space, the total rates are much more sensitive to the electron polarization. For instance, assuming $P_e = -1$ ($P_e = +1$) the total rate increases (decreases) by about 94% at $\sqrt{s} = 500$ GeV.

Some insight into this result can be gained by looking at Tables II and III, where the e/γ polarization dependence of the interference pattern of the $\gamma\gamma H$, $Z\gamma H$, and box contributions is shown for $p_T^e > 10$ GeV and $p_T^e > 100$ GeV, respectively, at $\sqrt{s} = 500$ GeV. For instance, one can see that for $P_e = +1$ there is a strong destructive interference between the terms $\gamma\gamma H$ and $Z\gamma H$. This is essentially due to the different sign of the couplings $ee\gamma$ and $e_R e_R Z$, where e_R stands for the right-handed electron component (see also Sec. II).

The fact that a longitudinal polarization of the electron beam affects drastically the large p_T^e range can also be clearly seen in Fig. 12, where the p_T^e distributions relative to the unpolarized and to the left-handed and right-handed polarized e beam are presented for the signal and the $e\gamma \to eb\bar{b}$ background. One can also see that, although both the signal S and background B are increased by a left-handed polarization, the ratio S/B is improved at large p_T^e.

Figures 13(a)–13(d) show the effects of assuming a longitudinally polarized photon beam in the same framework of Fig. 11. The trend is similar to the polarized e case, but the effect is quantitatively more modest for a polarized γ, especially at large values of $\sqrt{s}$. The only exception is given by the box contribution that is still considerably altered by $P_\gamma \neq 0$ at any $\sqrt{s}$.

VI. INITIAL-STATE RADIATION EFFECTS

The effects of the ISR on the signal and the background rates can be taken into account by folding the corresponding cross sections with a structure function describing the reduction of the electron beam energy because of the QED radiation. We adopt the approach of [29], that is accurate at the next-to-leading order for collinear emission and resums soft photon effects. All this is implemented through the computer package CompHEP, which automatically takes into account also the kinematical cuts needed either to enhance the $Z\gamma H$ contribution in the signal (i.e., p_T^e cuts) or to decrease the relative importance of the background (i.e., $\theta_{b\text{ beam}}$ cuts).

We compared the rates of the unfolded cross sections with the cross sections convoluted with the ISR structure function. The effect of the ISR in our context has been found to be

TABLE II. Interference pattern between the $\gamma\gamma Z$, $Z\gamma H$, and box contributions versus the e-beam and γ-beam polarizations, for $p_T^e > 10$ GeV.

$\sqrt{s}=$	m_H	$\sigma(e\gamma\to eH,\ p_T^e>10$ GeV) (fb)						
500 GeV	(GeV)	Total	$\lvert\gamma\gamma H\rvert^2$	$\lvert Z\gamma H\rvert^2$	$\lvert\text{box}\rvert^2$	Int.$_{(\gamma\gamma H - Z\gamma H)}$	Int.$_{(\gamma\gamma H\ \text{box})}$	Int.$_{(Z\gamma H\ \text{box})}$
($P_e=0$;	80	1.97	1.49	0.199	0.0576	0.0758	0.0797	0.0654
$P_\gamma=0$)	100	2.11	1.60	0.212	0.0623	0.0812	0.0854	0.0702
	120	2.37	1.80	0.233	0.0702	0.0903	0.0951	0.0782
	140	2.86	2.19	0.274	0.0859	0.108	0.114	0.0936
($P_e=-1$;	80	2.96	1.49	0.239	0.115	0.824	0.153	0.136
$P_\gamma=0$)	100	3.17	1.60	0.254	0.124	0.883	0.164	0.146
	120	3.55	1.80	0.280	0.140	0.981	0.182	0.163
	140	4.27	2.19	0.329	0.171	1.17	0.219	0.194
($P_e=+1$;	80	0.982	1.49	0.159	4.60×10^{-4}	-0.672	6.73×10^{-3}	-5.41×10^{-3}
$P_\gamma=0$)	100	1.05	1.60	0.169	4.79×10^{-4}	-0.720	7.17×10^{-3}	-5.74×10^{-3}
	120	1.19	1.80	0.187	5.08×10^{-4}	-0.801	7.83×10^{-3}	-6.25×10^{-3}
	140	1.45	2.19	0.219	5.53×10^{-4}	-0.956	8.96×10^{-3}	-7.08×10^{-3}
($P_e=0$;	80	2.18	1.49	0.206	0.104	0.172	0.108	0.101
$P_\gamma=-1$)	100	2.36	1.60	0.220	0.114	0.195	0.118	0.110
	120	2.67	1.80	0.244	0.130	0.232	0.136	0.126
	140	3.26	2.19	0.287	0.161	0.298	0.170	0.156
($P_e=0$;	80	1.76	1.49	0.191	0.0109	-0.0200	0.0516	0.0302
$P_\gamma=+1$)	100	1.87	1.60	0.203	0.0108	-0.0326	0.0524	0.0302
	120	2.07	1.80	0.223	0.0107	-0.0513	0.0540	0.0305
	140	2.47	2.19	0.261	0.0107	-0.0821	0.0575	0.0315

marginal in general. In particular, we found that the ISR effects slightly reduce the signal for all the electron polarization states. For the kinematical configurations described in Table I, bottom half, the signal is reduced by about 3%, for $p_T^e > 100$ GeV and even less (about 1%) for $p_T^e > 10$ GeV. On the other hand, the irreducible $e\gamma\to eb\bar{b}$ background is enhanced a little by the ISR. For $p_T^e > 100$ GeV, it is increased by less than 1%, while, for $p_T^e > 10$ GeV, it is raised by about 4%. This holds for both $P_e=0$ and $P_e=\pm1$.

We checked that such behaviors can be easily explained in terms of the increasing and/or decreasing of the relevant cross section with $\sqrt{s}$, when all the relevant kinematical cuts are taken into account.

Altogether, one can conclude that the ''unfolded'' general picture is only mildly modified by the ISR effects.

VII. OPTIMIZATION OF *S/B* AND ELECTRON ASYMMETRIES

As can be seen in Table I, bottom part, a p_T^e cut of 100 GeV, along with a resolution on $m_{b\bar{b}}$ of ±3 GeV and a cut on all the b's that are closer than 18° to the beams, optimizes the S/B ratio, for $m_H = 120$ GeV and $\sqrt{s} = 500$ GeV. In particular, it gives rise to a signal rate of 0.53 (1.0) fb versus an irreducible background rate of 0.63 (0.96) fb in the unpolarized ($P_e=-1$ polarized) case. This means that the signal and the background are comparable in the interesting configurations. With an integrated luminosity of 100 pb^{-1}, the corresponding statistical significance of the signal from $e\gamma\to eH$ is of the order $S/\sqrt{S+B}\simeq 5$ for $P_e=0$ and 7, if $P_e=-1$. This implies the possibility of measuring the corresponding cross section for $e\gamma\to eH$ with an accuracy of about 20% (15% for the polarized $P_e=-1$ beam), unless systematic errors dominate.

Of course, the final accuracy on the determination of the coupling of the Higgs boson to the Z and γ is not simply the accuracy on the cross-section measurement. As we can see from Table III, for $p_T^e > 100$ GeV and $\sqrt{s} = 500$ GeV (and unpolarized beams), the $Z\gamma H$ vertex contributes about half of the measured cross sections, including the interference effects. Assuming that the Higgs-boson coupling with the photons is tested and measured with high accuracy in some different process, the statistical sensitivity to the Higgs coupling with the Z and γ gets of the order $\frac{1}{2}S/\sqrt{S+B}$ (note that, assuming a reduced integrated luminosity of r100 fb^{-1}, with $r<1$, would in general lower the expected accuracy by a factor $\sqrt{r}$).

There is a further way to improve the accuracy on the cross-section measurement. This is by exploiting the electron angular asymmetry of the signal with respect to the beam. Indeed, we found that in the $e\gamma\to eb\bar{b}$ background the final electron angular distribution, although not completely symmetric, is almost equally shared in the forward and backward directions with respect to the beam. In particular, we checked that the second diagram in Fig. 8 is responsible for the backward peak, while the fourth diagram gives the forward one.

TABLE III. Interference pattern between the $\gamma\gamma Z$, $Z\gamma h$, and box contributions versus the e-beam and γ-beam polarizations, for $p_T^e > 100$ GeV.

$\sqrt{s}=$ 500 GeV	m_H (GeV)	$\sigma(e\gamma \to eH,\ p_T^e > 100\ \mathrm{GeV})$ (fb) Total	$\lvert\gamma\gamma h\rvert^2$	$\lvert Z\gamma h\rvert^2$	$\lvert \mathrm{box}\rvert^2$	$\mathrm{Int.}_{(\gamma\gamma h - Z\gamma h)}$	$\mathrm{Int.}_{(\gamma\gamma h\ \mathrm{box})}$	$\mathrm{Int.}_{(Z\gamma h\ \mathrm{box})}$
$(P_e=0;$	80	0.618	0.264	0.146	0.0451	0.0389	0.0651	0.0585
$P_\gamma=0)$	100	0.652	0.277	0.154	0.0481	0.0409	0.0695	0.0625
	120	0.705	0.296	0.166	0.0532	0.0439	0.0766	0.0692
	140	0.818	0.341	0.190	0.0633	0.0505	0.0909	0.0822
$(P_e=-1;$	80	1.20	0.264	0.176	0.0899	0.423	0.124	0.122
$P_\gamma=0)$	100	1.27	0.277	0.185	0.0959	0.445	0.133	0.130
	120	1.37	0.296	0.199	0.106	0.478	0.147	0.144
	140	1.59	0.341	0.228	0.126	0.549	0.174	0.171
$(P_e=+1;$	80	0.0371	0.264	0.117	3.55×10^{-4}	-0.345	5.86×10^{-3}	-4.94×10^{-3}
$P_\gamma=0)$	100	0.0386	0.277	0.123	3.66×10^{-4}	-0.363	6.21×10^{-3}	-5.22×10^{-3}
	120	0.0405	0.296	0.133	3.82×10^{-4}	-0.390	6.72×10^{-3}	-5.65×10^{-3}
	140	0.0465	0.341	0.152	4.10×10^{-4}	-0.448	7.62×10^{-3}	-6.36×10^{-3}
$(P_e=0;$	80	0.796	0.264	0.153	0.0798	0.118	0.0903	0.0901
$P_\gamma=-1)$	100	0.852	0.277	0.162	0.0860	0.131	0.0986	0.0983
	120	0.940	0.296	0.175	0.0962	0.149	0.112	0.112
	140	1.12	0.341	0.201	0.116	0.182	0.138	0.137
$(P_e=0;$	80	0.440	0.264	0.139	0.0104	-0.0403	0.0399	0.0268
$P_\gamma=+1)$	100	0.452	0.277	0.146	0.0103	-0.0487	0.0403	0.0267
	120	0.470	0.296	0.157	0.0101	-0.0610	0.0411	0.0268
	140	0.520	0.341	0.179	0.0101	-0.0812	0.0434	0.0275

On the contrary, the final electron in $e\gamma \to eH$ is mostly directed in the forward direction. The typical behavior is shown in Fig. 14, where the solid (dashed) line gives the histogram for the final electron angular distribution (in the center-of-mass system) for the signal (background), for $p_T^e > 100$ GeV and $\theta(b\ \mathrm{beam}) > 18°$, at $m_H = 120$ GeV and $\sqrt{s} = 500$ GeV. As usual, the background is integrated over the range $m_H - \Delta m_{b\bar{b}} < m_{b\bar{b}} < m_H + \Delta m_{b\bar{b}}$ with $\Delta m_{b\bar{b}} = 3$ GeV. The initial beams are assumed to be unpolarized. The strong asymmetry in the signal θ_e distribution is manifest. The final electron is mostly scattered forward in $e\gamma \to eH$ (the empty intervals for $\theta_e \lesssim 25°$ and $\theta_e \gtrsim 155°$ are just due to the $p_T^e > 100$ GeV cut). Note that this pattern keeps valid also when relaxing the p_T^e cut, and for polarized beams.

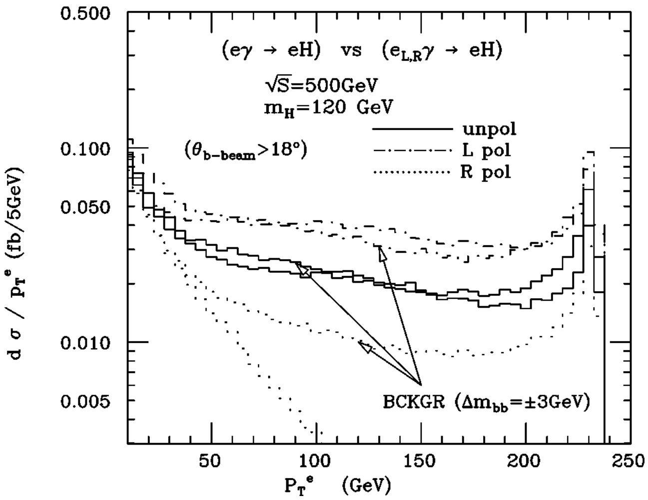

FIG. 12. Electron-beam polarization effects on the p_T^e distributions.

It is straightforward at this point to enhance the S/B ratio, by simply measuring the difference between the forward and backward cross sections. In Table IV, after applying the same cuts as in Table I, bottom part, and for different polarizations of the e beam, we report apart from the total rate, the forward cross sections and the difference of the forward and backward cross sections $\mathcal{S}_{\mathrm{FB}} = \sigma(\theta_e < 90°) - \sigma(\theta_e > 90°)$. One can see that, in the difference $\mathcal{S}_{\mathrm{FB}}$, 60% of the signal survives, while the background is reduced by about an order of magnitude, in both the interesting $P_e = 0$ and $P_e = -1$ cases. With a luminosity of 100 fb^{-1}, one then gets an accuracy on $\mathcal{S}_{\mathrm{FB}}$ of about 16% for unpolarized e beams, and 12% for $P_e = -1$ (corresponding to $S/\sqrt{S+B} \simeq 6.4$ and 8.5, respectively.) By the way, it could also be convenient to measure the relative asymmetry $\mathcal{S}_{\mathrm{FB}}/[\sigma(\theta_e < 90°) + \sigma(\theta_e > 90°)]$ that has the advantage of being free from possible uncertainties on the absolute normalization of the cross sections.

The analysis above can be also extended to the study of possible anomalous contributions in the $Z\gamma H$ amplitude coming from some extension of the standard model. For instance, all models causing a variation in the cross section and/or angular asymmetries by more than about 20% should

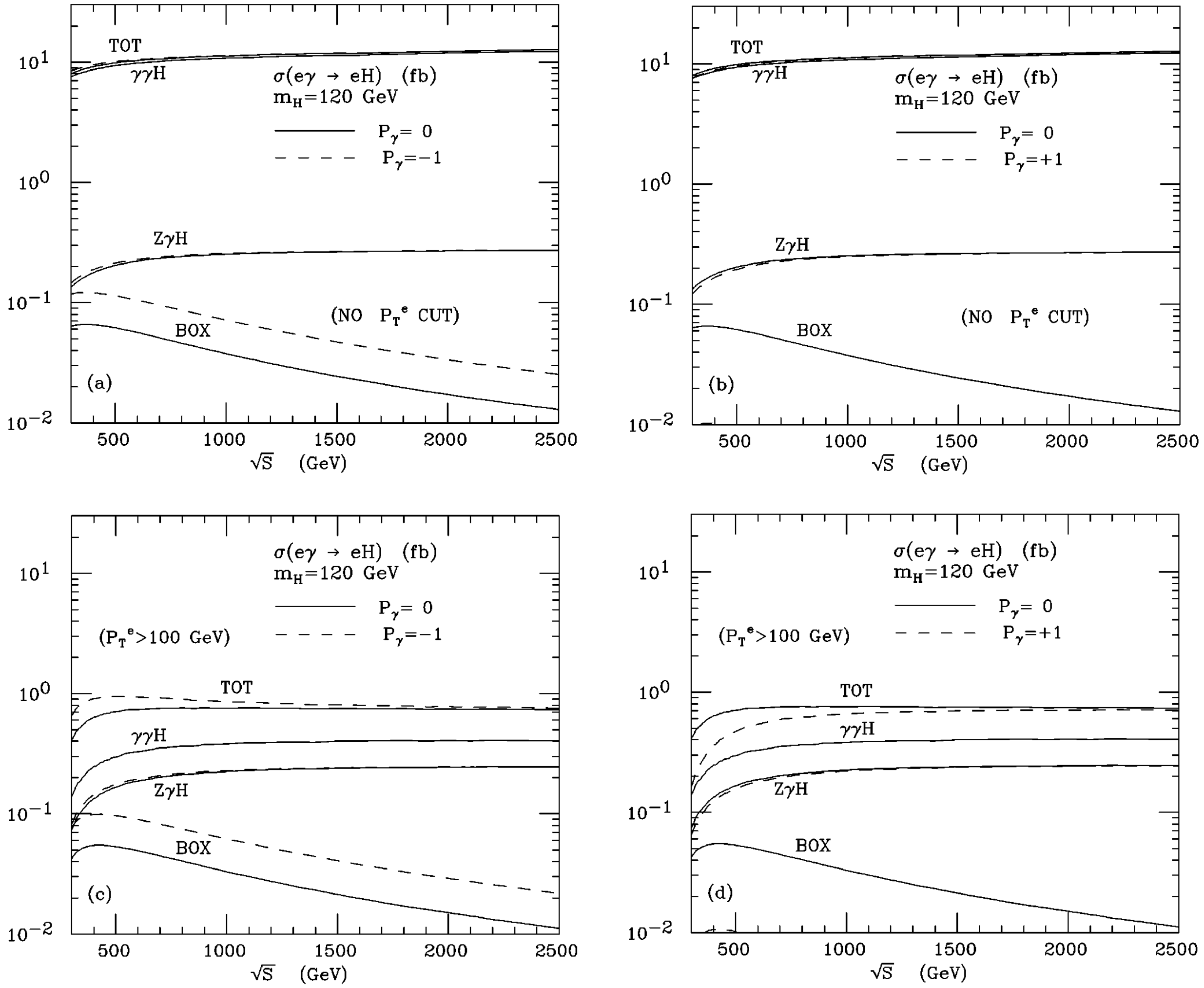

FIG. 13. Photon-beam polarization effects without [(a) and (b)] and with [(c) and (d)] a cut $p_T^e > 100$ GeV.

be easily disentangled in the same experimental conditions analyzed here. Furthermore, since in the latter case what we call here signal could act as a further background, it could be convenient to consider also the $P_e = +1$ cross sections [35]. Indeed, as shown in Table III, for large p_T^e the right-handed polarized e beam minimizes the standard model $e\gamma \to eH$ *background*, because of the strong negative interferences between the different amplitudes.

VIII. CONCLUSIONS

The study of the exact rates for the process $e\gamma \to eH \to e(b\bar{b})$ in the intermediate m_H range confirms that the associated He production in $e\gamma$ collisions is a competitive means with respect to the process $\gamma\gamma \to H$ to study the vertex $\gamma\gamma H$ and its possible anomalies (as anticipated by the analysis made in the WW approximation [15]). The relevant total (unpolarized) cross sections are in the range (9–17) fb, for $m_H = (90-150)$ GeV and $\sqrt{s} = (0.5-1.5)$ GeV, which, assuming an integrated luminosity of 100 fb^{-1}, corresponds to $\sim 10^3$ Higgs events.

If the final electron is tagged at large p_T^e, a further possi-

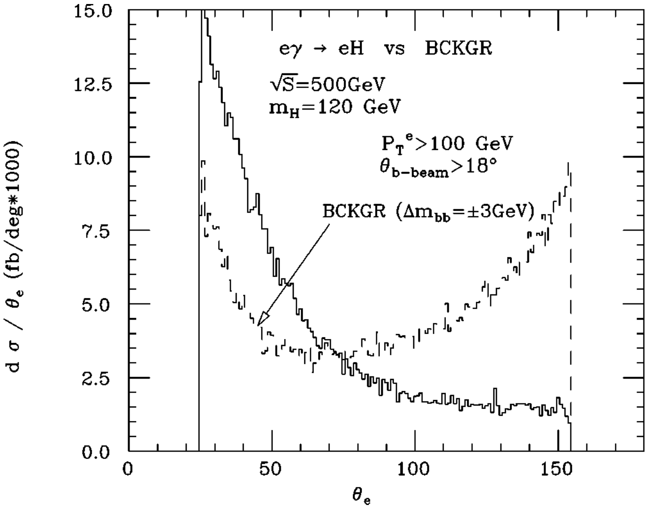

FIG. 14. Final electron angular distribution with respect to the initial electron beam. The solid (dashed) line refers to the signal (irreducible $e\gamma \to eb\bar{b}$ background). The kinematical cuts applied are shown in the plot. The initial beams are assumed to be unpolarized.

TABLE IV. Forward-backward asymmetry in the electron scattering angle, θ_e, for different e-beam polarizations. The total cross section, the forward cross section, and the difference of the forward and backward cross sections $[\mathcal{S}_{\mathrm{FB}}=\sigma(\theta_e<90°)-\sigma(\theta_e>90°)]$ for the signal and the irreducible background, are presented. The kinematical cuts $\theta_{b\ \mathrm{beam}}>18°$, $P_t^e>100$ GeV, and $m_H-\Delta m_{b\bar{b}}<m_{b\bar{b}}<m_H+\Delta m_{b\bar{b}}$, with $\Delta m_{b\bar{b}}=3$ GeV, are applied.

$m_H=120$ GeV	$\sigma(e\gamma\to eH)$ fb			$\sigma(e\gamma\to eb\overline{b)}$ fb		
$\sqrt{s}=500$ GeV	No θ_e cut	$\theta_e<90°$	$\mathcal{S}_{\mathrm{FB}}$	No θ_e cut	$\theta_e<90°$	$\mathcal{S}_{\mathrm{FB}}$
$P_e=0$	0.530	0.425	0.320	0.634	0.281	-0.072
$P_e=-1$	1.03	0.820	0.610	0.961	0.433	-0.095
$P_e=1$	0.0249	0.0245	0.0241	0.304	0.126	-0.052

bility offered by the channel $e\gamma\to eH$ is to study the effects coming from the $Z\gamma H$ vertex, still keeping a reasonable statistics $[\sim 10^2$ events]. This possibility does not have any counterpart in the e^+e^- and $\gamma\gamma$ collision physics. Graphs with boxes, too, contribute at large p_T^e, but their relative importance decreases with $\sqrt{s}$ for $\sqrt{s}>400$ GeV.

We checked that the main background comes from the process $e\gamma\to eb\overline{b}.$ This can be controlled by a good $m_{b\bar{b}}$ experimental resolution (that can be improved by the final electron energy determination), and by requiring that the final b quarks not be too close to the beam's direction.

We have also shown that starting with a left-handed polarized electron beam doubles the rates and improves the S/B ratio, in the $p_T^e\gtrsim 100$ GeV kinematical range interesting for the $Z\gamma H$ vertex studies. Further improvements in the S/B ratio can be obtained by exploiting the final-electron angular asymmetry of the signal. The inclusion of the initial-state radiation effects marginally deteriorates the S/B ratio.

The value of the integrated luminosity assumed in this study (that is 100 fb^{-1}) does not seem to be essential to disentangle a $Z\gamma H$ effect, although a high luminosity would be crucial to increase the accuracy of the measurement. With a luminosity of 100 fb^{-1}, one expects an accuracy as good as about 10% on the measurement of the $Z\gamma H$ effects, at $\sqrt{s}=500$ GeV. A luminosity of 50 fb^{-1} would anyhow allow one to measure the standard model signal with an accuracy better than 20%.

In conclusion, the $e\gamma\to eH\to e(b\overline{b)}$ turns out to be an excellent means to check the standard-model one-loop coupling $Z\gamma H$. Further investigation and comparison with the predictions from possible extensions of the standard model altering the $Z\gamma H$ vertex is worthwhile. This, we are planning to do in a forthcoming paper [35].

ACKNOWLEDGMENTS

Useful discussions with I. F. Ginzburg and A. E. Pukhov are gratefully acknowledged. The work of V.A.I. was partly supported by Grant Nos. INTAS-93-1180ext and 96-02-18635 from the Russian Fund for Basic Research. V.A.I. wishes also to thank INFN for its hospitality and the possibility to work during his visit at the University of Roma 1.

APPENDIX

In this appendix, we give the explicit expressions for the functions B_0, C_0, and D_i appearing in Eqs. (15), (20), and (21). Next, we give a short discussion on some sources of numerical instabilities arising in the computation of the total cross section, and describe the method used to control them.

1. Loop integrals

The complete set of independent loop integrals used in our calculations is defined by the following formulas in dimensional regularization,[7] where the time-space dimension is $n=4-2\varepsilon$:

$$B_0(p^2,m^2,m^2)\equiv\frac{1}{i\pi^2}\int\frac{d^nq}{[m^2-q^2][m^2-(q+p)^2]},\tag{A1}$$

$$C_0(m,p_1,m,p_2,m)$$
$$\equiv\frac{1}{i\pi^2}\int\frac{d^nq}{[m^2-q^2][m^2-(q+p_1)^2][m^2-(q+p_2)^2]},\tag{A2}$$

$$D_{0;\mu;\mu\nu}(m_0,p_1,m_1,\ldots,p_3,m_3)$$
$$\equiv\frac{1}{i\pi^2}\int\frac{\{1;q_\mu;q_\mu q_\nu\}d^nq}{[m_0^2-q^2][m_1^2-(q+p_1)^2]\cdots[m_3^2-(q+p_3)^2]}.\tag{A3}$$

Of course, each denominator factor originated from the propagators should be treated in the Feynman limit: $(M^2-p^2)^{-1}\equiv\lim_{\epsilon\to 0}(M^2-p^2-i\epsilon)^{-1}$. As a result, these loop integrals have complex values in general.

We decompose the vector and tensor box integrals over the covariant Lorentz structures:

---

[7] Relations to other definitions of one-loop integrals: Our definition of integrals corresponds to the *Passarino-Veltman* integrals [30] if the metric signature is changed from $(-+++)$, used by Passarino-Veltman, to $(+---)$. They also used a different choice of external momenta, hence their decomposition (A4) differs from ours. We differ from [31] by an opposite sign of the C integrals.

$$D^{\mu} \equiv p_1^{\mu} \cdot D_1 + p_2^{\mu} \cdot D_2 + p_3^{\mu} \cdot D_3,$$

$$\begin{aligned} D^{\mu\nu} \equiv{}& g^{\mu\nu} \cdot D_{00} + p_1^{\mu} p_1^{\nu} \cdot D_{11} + p_2^{\mu} p_2^{\nu} \cdot D_{22} + p_3^{\mu} p_3^{\nu} \cdot D_{33} \\ &+ (p_1^{\mu} p_2^{\nu} + p_2^{\mu} p_1^{\nu}) \cdot D_{12} + (p_1^{\mu} p_3^{\nu} + p_3^{\mu} p_1^{\nu}) \cdot D_{13} \\ &+ (p_2^{\mu} p_3^{\nu} + p_3^{\mu} p_2^{\nu}) \cdot D_{23}. \end{aligned} \tag{A4}$$

Note that all these integrals are UV finite. The only exception is B_0, for which $\lim_{\varepsilon \to 0} \varepsilon B_0 = 1$. In our results, the integrals B_0 appear in the triangle contributions only in a UV finite combination [see Eq. (15)].

For the numerical evaluation of the scalar loop integrals, as well as of the scalar factors in the decomposition (A4), we used the FF library [32], and the corresponding Fortran routines. Note that in our definition of the loop integrals, the C-type integrals have an opposite sign with respect to the latter. Moreover, in the decomposition (A4) we use a set of external momenta different from the FF library. Hence, we perform a linear transformation of our scalar factors D_i and D_{ij}, in order to get a connection with the corresponding factors defined in the FF library.

Regarding the analytical evaluation of the amplitudes, the check of the QED gauge-invariance identities (6), as well as the extraction of the QED gauge noninvariant terms (22) and the corresponding ones coming from the W-box diagrams, we used the computer algebra system REDUCE [33].

2. Numerical instabilities

Although, in general, we computed the relevant amplitudes in the $m_e = 0$ chiral limit, in the calculation of the total cross section we assumed for $t_{\max}$ the exact value, that is approximately equal to $(-m_e^2 m_H^4 / s^2)$. Then, when integrating the region near the t-channel pole at $t \simeq 0$ with routines in double precision for arithmetic operations, we met some numerical instabilities. In particular, we observed a loss of numerical precision in the evaluation of the kinematics for $t \geqslant -10^{-9}$ GeV^2. In order to avoid this instability, we used the following procedure. We introduced some parameter t_0 and approximated the matrix element M for the t-channel photon contribution by $M = X(t)/t$ for $t \leqslant t_0$, and $M = X(t_0)/t$ for $t_0 \leqslant t \leqslant t_{\max}$, where $X(t)$ is the numerator of the matrix element. If the parameter t_0 is taken close to $t_{\max}$, the latter turns out to be a good approximation, since then $X(t_{\max})$ differs very little from $X(t_0)$. To test this method, we checked the independence of the total cross section from the parameter t_0, by varying t_0 in the interval $-1 \leqslant t_0 \leqslant -10^{-6}$ GeV^2.

There is also a second source of numerical instability when the W- and Z-box diagrams are evaluated near $t = 0$ and $u = 0$. When the tensor integrals for the boxes are expressed via the scalar integrals by Passarino and Veltman [30] (e.g., FF library uses this procedure [32]) some spurious poles can arise from different terms. Of course, in the total results these poles cancel each other. In our case such spurious poles arise at $t = 0$ and $u = 0$. We checked analytically the corresponding cancellation in our results for the boxes (18) and (19). First, we expressed the formulas (19) via scalar integrals and then analyzed the final expressions in $t = 0$ and $u = 0$, where they must vanish. This analysis was made with the help of the REDUCE program PV [34], that implements the Passarino-Veltman procedure. Anyhow, it is not possible to check explicitly the cancellation of these spurious poles at the level of the scalar integrals. As a result, these integrals cannot be evaluated with good accuracy at $t \geqslant -10^{-6}$ GeV^2, since the numerical precision of the FF library is not sufficient to get this cancellation. Fortunately, one can neglect the box contributions at such small t and u, since these functions have a regular behavior near $t = 0$ and $u = 0$. Therefore, we just neglected the W- and Z-box contributions for $t, u \geqslant -10^{-2}$ GeV^2.

[1] A. Blondel, *Proceedings, ICHEP'96, Warsaw, 1996* (World Scientific, Singapore, 1997).

[2] Proceedings, in *Physics and Experiments with e^+e^- Linear Colliders*, Saariselkä, 1991, edited by R. Orava, P. Eerola, and M. Nordberg (World Scientific, Singapore, 1992); in *Proceedings of Physics and Experiments with e^+e^- Linear Colliders*, Waikoloa, Hawaii, 1993, edited by F. Harris, S. Olsen, S. Pakvasa, and X. Tata (World Scientific, Singapore, 1993); in *Proceedings of Physics and Experiments with e^+e^- Linear Colliders*, Morioka, 1995, edited by A. Miyamoto, Y. Fujii, T. Matsui, and S. Iwata (World Scientific, Singapore, 1996).

[3] *e^+e^- Collisions at 500 GeV: The Physics Potential*, Proceedings of the Workshop, Münich, Annecy, Hamburg, 1991, edited by P. Zerwas (DESY Report No. 92-123A, B. Hamburg, 1992); *e^+e^- Collisions at 500 GeV: The Physics Potential*, Proceedings, edited by P. Zerwas (DESY Report No. 93-123C, Hamburg, 1993); *e^+e^- Collisions at 500 GeV: The Physics Potential*, Proceedings, edited by P. Zerwas (DESY Report No. 96-123D, Hamburg, 1996).

[4] I.F. Ginzburg, G.L. Kotkin, V.G. Serbo, and V.I. Telnov, Nucl. Instrum. Methods Phys. Res. **205**, 47 (1983); I.F. Ginzburg, G.L. Kotkin, S.L. Panfil, V.G. Serbo, and V.I. Telnov, *ibid.* **219**, 5 (1984); V.I. Telnov, Nucl. Instrum. Methods Phys. Res. A **294**, 72 (1990).

[5] *Proceedings of the Workshop of Gamma-Gamma Colliders*, Berkeley, California, 1994 [Nucl. Instrum. Methods Phys. Res. A **355**, 19 (1995)].

[6] J.F. Gunion, H.E. Haber, G.L. Kane, and S. Dawson, *The Higgs Hunter's Guide* (Addison-Wesley, New York, 1990).

[7] H.M. Georgi, S.L. Glashow, M.E. Machacek, and D.V. Nanopoulos, Phys. Rev. Lett. **40**, 692 (1978); A. Djouadi, M. Spira, and P.M. Zerwas, Phys. Lett. B **264**, 440 (1991); S. Dawson, Nucl. Phys. **B359**, 283 (1991); M. Spira, A. Djouadi, D. Graudenz, and P.M. Zerwas, *ibid.* **B453**, 17 (1995)

[8] J. Ellis, M.K. Gaillard, and D.V. Nanopoulos, Nucl. Phys. **B106**, 292 (1976); M.A. Shifman, A.I. Vainshtein, M.B. Voloshin, and V.I. Zakharov, Sov. J. Nucl. Phys. **30**, 711 (1979).

[9] L. Bergstrom and G. Hulth, Nucl. Phys. **B259**, 137 (1985); **B276**, 744(E) (1986).

[10] F. Wilczek, Phys. Rev. Lett. **39**, 1304 (1977).

[11] A. Djouadi, V. Driesen, W. Hollik, and A. Kraft, e-print KA-TP-30-1996, PM/96-39, hep-ph/9701342.

[12] J.F. Gunion and H.E. Haber, Phys. Rev. D **48**, 5109 (1993); O.J.P. Èboli, M.C. Gonzales-Garcia, F. Halzen, and D. Zeppenfeld, *ibid.* **48**, 1430 (1993); D.L. Borden, D.A. Bauer, and D.O. Caldwell, *ibid.* **48**, 4018 (1993); D.L. Borden, V.A. Khoze, W.J. Stirling, and J. Ohnemus, *ibid.* **50**, 4499 (1994); M. Baillargeon, G. Belanger, and F. Boudjema, *ibid.* **51**, 4712 (1995).

[13] I. Watanabe, *Proceedings of Physics* $e^+e^-, e\gamma$ *and* $\gamma\gamma$ *collisions at linear accelerators,* Tokyo, 1994, hep-ph/9504226.

[14] C.F. von Weizsäcker, Z. Phys. **88**, 612 (1934); E.J. Williams, Phys. Rev. **45**, 729 (1934).

[15] O.J.P. Èboli and M.C. Gonzales-Garcia, Phys. Rev. D **49**, 91 (1994).

[16] D.A. Dicus and W.W. Repko, Phys. Rev. D **53**, 3616 (1996).

[17] A. Barroso, J. Pulido, and J.C. Romao, Nucl. Phys. **B267**, 509 (1985); *ibid.* **B272**, 693 (1986).

[18] A. Abbasabadi, D. Bowser-Chao, D.A. Dicus, and W.A. Repko, Phys. Rev. D **52**, 3919 (1995).

[19] A. Djouadi, V. Driesen, W. Hollik, and J. Rosiek, Nucl. Phys. **B491**, 68 (1997).

[20] A. Denner, J. Kublbeck, R. Mertig, and M. Bohm, Z. Phys. C **56**, 261 (1992).

[21] W. Buchmüller and D. Wyler, Nucl. Phys. **B268**, 621 (1986).

[22] K. Hagiwara *et al.*, Phys. Rev. D **48**, 2182 (1993).

[23] E.E. Boos, M.N. Dubinin, V.A. Ilyin, G.V. Jikia, A.E. Pukhov, and S.F. Sultanov, Phys. Lett. B **273**, 173 (1991); K. Hagiwara, I. Watanabe, and P.M. Zerwas *ibid.* **278**, 187 (1992); K. Cheung, Phys. Rev. D **48**, 1035 (1993); E. Boos, A. Pukhov, M. Sachwitz, and H.J. Schreiber, Z. Phys. C **75**, 237 (1997).

[24] V. I. Telnov, Communication to the Final Meeting of the Joint ECFA/DESY LC Study on Physics and Detectors for a Linear Collider, DESY, 1996, Hamburg (unpublished).

[25] P. A. Baikov *et al.*, hep-ph/9701412; E.E. Boos, M.N. Dubinin, V.A. Ilyin, A.E. Pukhov, and V.I. Savrin, Report No. SNUTP-94-116, hep-ph/9503280.

[26] V.M. Budnev *et al.*, Phys. Rep. **15C**, 181 (1975); S. Frixione, M. Mangano, P. Nason, and G. Ridolfi, Phys. Lett. B **319**, 339 (1993).

[27] P. Mättig, Status Report of a Study on Higgs & Photon Production in 500 GeV e^+e^- Collisions, memorandum, 1995 (unpublished).

[28] M. Glück, E. Reya, and A. Vogt, Phys. Rev. D **46**, 1973 (1992).

[29] E.A. Kuraev and V.S. Fadin, Sov. J. Nucl. Phys. **41**, 466 (1985); S. Jadach, B.F.L. Ward, Comput. Phys. Commun. **56**, 351 (1990).

[30] G. Passarino and M. Veltman, Nucl. Phys. **B160**, 151 (1979).

[31] A. Denner, Fortschr. Phys. **41**, 307 (1993).

[32] G.J. van Oldenborgh, ''FF—a package to evaluate one-loop Feynman diagrams,'' NIKHEF-H/90-15, 1990; G.J. van Oldenborgh and J.A.M. Vermaseren, Z. Phys. C **46**, 425 (1990).

[33] A. Hearn, J. Fitch REDUCE User's Manual, Vol. 3.6 (RAND, City, 1995).

[34] V.A. Ilyin and A.P. Kryukov, Report No. INP MSU 97-5/456, 1997.

[35] E. Gabrielli, V.A. Ilyin, and B. Mele (in preparation).